Received: 19 December 2019 | Accepted: 14 May 2020

DOI: 10.1002/hyp.13838

USING WATER AGE TO EXPLORE HYDROLOGICAL PROCESSES IN CONTRASTING ENVIRONMENTS

WILEY

Isotope-aided modelling of ecohydrologic fluxes and water ages under mixed land use in Central Europe: The 2018 drought and its recovery

Aaron Smith[1] | Doerthe Tetzlaff[1] | Lukas Kleine[1,2] | Marco P. Maneta[4] | Chris Soulsby[3]

[1]Department of Ecohydrology, IGB Leibniz Institute of Freshwater Ecology and Inland Fisheries Berlin, Berlin, Germany

[2]Geographisches Institut, Humboldt University Berlin, Berlin, Germany

[3]Northern Rivers Institute, School of Geosciences, University of Aberdeen, Aberdeen, UK

[4]School of Geosciences, University of Montana, Missoula, Montana, USA

Correspondence
Aaron Smith, Department of Ecohydrology, IGB Leibniz Institute of Freshwater Ecology and Inland Fisheries Berlin, Müggelseedamm 310, 12587, Berlin, Germany.
Email: smith@igb-berlin.de

Abstract

Understanding the interactions of vegetation and soil water under varying hydrological conditions is crucial to aid quantitative assessment of land-use sustainability for maintaining water supply for humans and plants. Isolating and estimating the volume and ages of water stored within different compartments of the critical zone, and the associated fluxes of evaporation, transpiration, and groundwater recharge, facilitates quantification of these soil–plant-water interactions and the response of ecohydrological fluxes to wet and dry periods. We used the tracer-aided ecohydrological model EcH_2O-iso to examine the response of water ages of soil water storage, groundwater recharge, evaporation, and root-uptake at a mixed land use site, in northeastern Germany during the drought of 2018 and in the following winter months. The approach applied uses a dynamic vegetation routine which constrains water use by ecological mechanisms. Two sites with regionally typical land-use types were investigated: a forested site with sandy soils and a deep rooting zone and a grassland site, with loamier soils and shallower rooting zone. This results in much younger water ages (<1 year) through the soil profile in the forest compared to the grass, coupled with younger groundwater recharge. The higher water use in the forest resulted in a more pronounced annual cycle of water ages compared to the more consistent water age in the loamier soil of the grasslands. The deeper rooting zone of the forested site also resulted in older root-uptake water usage relative to soil evaporation, while the grassland site root-uptake was similar to that of soil evaporation. Besides more dynamic water ages in the forest, replenishment of younger soil waters to soil storage was within 6 months following the drought (cf. >8 months in the grassland). The temporal evaluation of the responsiveness of soil and vegetation interactions in hydrologic extremes such as 2018 is essential to understand changes in hydrological processes and the resilience of the landscape to the longer and more severe summer droughts predicted under future climate change.

KEYWORDS
Ecohydrological modelling, forest hydrology, isotopes, tracer-aided modelling, transit times, water ages

1 | INTRODUCTION

Many regions worldwide have been under increasing duress from warmer, drier summers, with long-term projections showing likely future exacerbation of these conditions (King & Karoly, 2017; Quesada, Vautard, Yiou, Hirschi, & Seneviratne, 2012). Longer-term climatic projections indicate more frequent droughts, which will negatively impact agricultural productivity with increased annual soil evaporation and transpiration ("green" water fluxes), with a complementary reduction in groundwater recharge ("blue" water fluxes) and annual water availability (Iglesias & Garrote, 2015; Orth & Destouni, 2018). In Europe, with increased occurrence of extreme heatwaves and long-term trends of decreasing soil moisture (Christidis, Jones, & Stott, 2014; Hanel et al., 2018; Schoetter, Cattiaux, & Douville, 2014), it is necessary to quantitatively examine how different species, vegetation communities, and land management strategies affect water partitioning to balance increased crop and timber production with reductions in blue fluxes and while maintaining ecosystem health (Teuling et al., 2010). There is a need to continuously assess the recovery time of different species/communities and soils under recurrent droughts to identify regions with high sustainability risk due to limited availability of green water sources (Ivits, Horion, Fensholt, & Cherlet, 2014; Schwalm et al., 2017). Consequently, future land use and agricultural planning will require an evidence base to inform the prioritization of vegetation management strategies. These strategies are needed to optimize yield under low soil moisture conditions while reducing the financial and ecological burden of abstraction (Berbel et al., 2019), and maintaining a balanced partitioning of green and blue water fluxes. To discern how long-term change will affect the coupling of green water fluxes with landscape storage dynamics, we need to investigate the current response of partitioning and recovery of fluxes and water ages following extreme events.

Examining the partitioning of ecohydrologic fluxes (evaporation and transpiration) and their accompanying water ages requires the use of ecohydrological models to isolate the effects of water availability and plant physiological processes (Newman et al., 2006). Without a sophisticated ecohydrological model or very large in situ datasets, accurate assessment of the partitioning of ecohydrological fluxes temporally and spatially with depth is difficult. While many hydrologic models can estimate evaporation and transpiration, the majority of these models do not consider the interaction of water stress and vegetation phenology (e.g., dynamic allocation to leaf growth) on transpiration. During drought conditions, the non-linearity of plant water usage becomes more important in assessing the role of different vegetation in exacerbating hydrological water stresses (Porporato, Laio, Ridolif, & Rodriguez-Iturbe, 2001).

Besides ecohydrologic models, stable isotopes of water, deuterium (δ^2H), and oxygen-18 ($\delta^{18}O$), and estimated water ages are useful tools to identify the partitioning of ecohydrologic fluxes at both the plot and catchment scale (Rothfuss et al., 2010; Tetzlaff et al., 2015). Incorporating isotope data into ecohydrological models can help model evaluation. For example, isotopic fractionation during evaporation can enrich soil waters and indicate the degree of soil evaporation relative to modelled soil moisture estimations, where over-enrichment indicates an overestimation of soil evaporation; and vice versa (Sprenger, Tetzlaff, & Soulsby, 2017; Sutanto, Wenninger, Coenders-Gerrits, & Uhlenbrook, 2012). Stable isotopes thus hold considerable potential for evaluating whether the modelled mixing mechanisms, flushing rates, and residence times of water in various storage components are consistent with processes operating in reality (Hrachowitz, Savenije, Bogaard, Tetzlaff, & Soulsby, 2013; Rinaldo et al., 2011). The model, EcH_2O-iso, incorporates the essential ecohydrologic fluxes governing water partitioning; tracks the isotopic composition of water in various storages and associated fluxes, conceptualizes various mixing processes; estimates the associated water ages; and has been applied and verified in a range of environments (Douinot et al., 2019; Kuppel, Tetzlaff, Maneta, & Soulsby, 2018a; Maneta & Silverman, 2013; Smith, Tetzlaff, Laudon, Maneta, & Soulsby, 2019). The evaluation of water ages is essential for both understanding and validating critical zone and atmospheric water sources and water recycling (Evaristo et al., 2019), storage and contamination vulnerability, sustainability of biological growth, and duration of soil chemical reactions (Sprenger et al., 2019). Despite the importance of vegetation for atmospheric recycling, there are limited studies quantifying ages of water used by vegetation (Sprenger et al., 2019), which are likely profoundly influenced by extreme conditions. As such, quantitative evaluation of the water age dynamics of soil water and vegetation water during extreme events is useful in interpreting the recovery (time until the system returns to more normal functional states), resilience (the ability of the system to maintain function during extreme events), and lethal water stress (no vegetation recovery) of an ecosystem. Water age has shown to be correlated with the water deficit caused by droughts and the recovery of "blue" water fluxes and storages in catchments (Stoelzle, Stahl, Morhard, & Weiler, 2014), and is useful in drought analysis with pre-drought water dominating the "blue" water fluxes and smaller rain events during drought used in "green" water fluxes (McGuire, DeWalle, & Gburek, 2002). The correlation of water age to catchment recovery during droughts may be due to storage-related lag times of "blue" water fluxes ("memory" effect) between inputs and outputs (e.g., 4-year recovery suggested Thomas, Lischeid, Steidl, & Dietrich, 2015) and the associated influence of vegetation

depending on these storages. However, the "memory" effect of extreme events is often site-specific and can highly depend on prevailing hydroclimate, soil properties (e.g., porosity and permeability) and vegetation species (e.g., rooting depth, water use efficiency, degree of stomatal control, etc.) (e.g., Walter et al., 2011).

The primary aim of this study was to assess the influence of drought and recovery on ecohydrologic fluxes and water ages of a mixed land use site during the 2018 drought in northeast Germany. In many parts of Europe, the drought of 2018 caused dramatically reduced crop yields and in some places forest dieback (Toreti et al., 2019). The drought provides an opportunity to couple uninterrupted field investigations including soil water stable isotopes (δ^2H and $\delta^{18}O$) with an isotope-aided ecohydrologic model (EcH_2O-iso) to assess: (a) the dynamics of ecohydrological fluxes of grasslands and forests during and following the drought; and (b) evaluate how water ages change in soil evaporation, transpiration, groundwater recharge and water storage under varying periods of drought and recovery. It was envisaged that quantifying the ecohydrologic partitioning and assessing resilience during and following the drought would enhance understanding of hydrological processes under drought and contribute to an evidence base for informing long-term land-use planning in drought-sensitive regions such as the North European plain where the study is based.

2 | MATERIALS AND METHODS

2.1 | Study site

The study site is in an agriculturally-dominated catchment, with long-term monitoring for hydrology and stream water chemistry, known as the Demnitzer Millcreek catchment (Smith, Tetzlaff, Gelbrecht, Kleine, & Soulsby, 2020). Situated in northeast Germany, the catchment is generally underlain by freely draining brown-earths and sandy soils over glacial drift containing deeper groundwaters. The catchment experiences a mid-continental climate with relatively low precipitation (557 mm average annual precipitation between 1981 and 2010, DWD, 2019) with higher precipitation during summers due to convective storms (317 mm average rainfall and 74% relative humidity in May–October between 1981 and 2010) and lower, less intense precipitation during winters (240 mm average rainfall and 81% relative humidity in November–April between 1981 and 2010).

The site has two high-resolution soil and vegetation monitoring plots situated in the mid-section of the catchment (Figure 1a). The two high-resolution monitoring plots are within 400 m (Figure 1b), encompassing a grassland site and forest site, with different soil properties but a negligible elevation difference (both sites at 54 m a.s.l.).

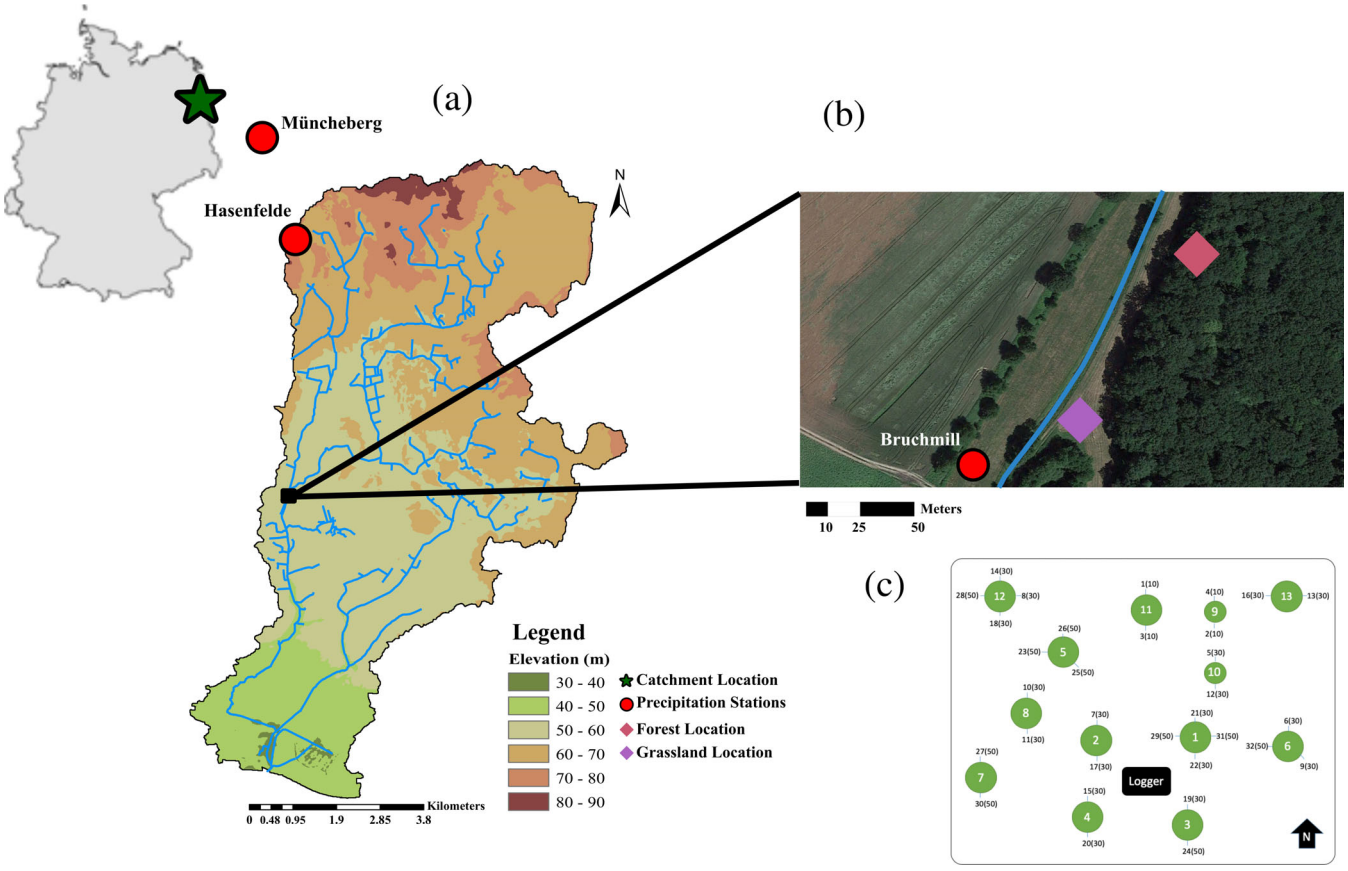

FIGURE 1 (a) Location of the Demnitzer Millcreek catchment (DMC) in Germany, and location of the grassland and forest study sites in the DMC, (b) location of the grassland and forest sites, (c) numbered trees (number in the circle) with sap flow sensor orientation and number (numbered ticks) in the forest site

The grassland site is characterized as a sandy loam, while the forest site is a loamy sand (podzolic brown-earth). While both sites show soil texture dominated by larger grain-sizes (>0.063 mm) the clay content in the surface horizons of the forest site (~3%) is around half that at the grassland site (7%) (Table 1). Soil moisture conditions between the sites reflect the soil textural differences, with more freely draining coarser soils in the forest resulting in generally lower soil moisture. The drawdown of soil moisture during the summer months is consistent with the higher summer evapotranspiration in the catchment (Smith et al., 2020).

The vegetation in the grassland is homogenous (10 m × 10 m fenced area) with relatively new growth of grass (*Echinochloa polystachya*) over a previously forested and ploughed soil. The grassland site is substantially sheltered by the adjacent forest to the south and east (Figure 1b) and receives less rainfall than the forest, and lower radiation because of the adjacent forest shading the southerly sun angle, and is protected from the prevailing south and easterly winds. The forest site has a variety of tree species including European oak (*Quercus robur*), Red oak (*Quercus rubra*), common hazel (*Corylus avellana*), and Scots Pine (*Pinus sylvestris*) with relatively even spacing throughout the forest plot (Figure 1c). The European oak is the most common tree in the plot, while the Scots Pine is the least common.

2.2 | The EcH$_2$O-iso model and model set-up

2.2.1 | EcH$_2$O-iso water balance

EcH$_2$O-iso is an ecohydrologic model based on core modules that integrate water balance, energy balance, carbon fixation and vegetation dynamics (Maneta & Silverman, 2013). The full description of the EcH$_2$O model structure and parameterisation is provided in Maneta and Silverman (2013) with a description of the isotope-related structure and parameterization provided in Kuppel et al. (2018a). Here we provide a synopsis of the key modules for the plot sites. In this study, we applied the model in 1-D at the two sites, the forest and grassland monitoring plots, using local data for each site to force, calibrate, and evaluate the model (Table 2). The water balance component of EcH$_2$O-iso is divided into three distinct storages: vegetation storage (canopy storage), ponded water, and soil storage. However, vegetation and ponded water storages are relatively minor, whereas the soil storage controls the primary hydrological functions. Soil storage is divided into three subsurface layers, with the first layer constraining infiltration and evaporation, and the third layer regulating recharge to the groundwater system. Infiltration to layer 1 is based on the Green-Ampt model (Mein & Larson, 1973), and is a function of the Brooks-Corey and air-entry pressure parameters, and the depth of soil layer 1 (top soil). Soil evaporation is constrained to the top soil layer, which assumes that the deepest extent of soil evaporation is the depth of soil layer 1. Vertical water flow between soil layers is based on a gravitational drainage model that permits downward flow when soil moisture exceeds field capacity. Downward flows occur at a rate controlled by the soil moisture excess. Gravitational drainage from layer 3 can leak downward through the bottom boundary of the layer or leave the plot via lateral groundwater outflow.

2.2.2 | EcH$_2$O-iso energy balance and vegetation dynamics

The energy balance in EcH$_2$O-iso is divided into canopy and surface energy balance components, which are solved sequentially. In the canopy, available radiative energy (net radiation) is partitioned into latent heat for transpiration and interception evaporation, and canopy sensible heat, by iteratively solving for the canopy temperature. Canopy interception latent heat is governed by the maximum canopy storage (CWS_{max}, Table 3), which controls the maximum water stored on the vegetation per leaf area index. The latent heat associated with

TABLE 1 Soil grain size properties at the grassland and forest sites and the average soil moisture content during the winter (November–April) and summer (May–October)

		Soil grain size distribution (%)				Average soil moisture		
	Depth (cm)	<0.002 mm	0.002–0.063 mm	0.063–0.63 mm	0.63–2.0 mm	Depth (cm)	Winter water content	Summer water content
Grassland	0–8	6.3	11.3	78.5	3.9	20	23.8	15.8
	8–28	7.7	11.0	76.5	4.8			
	28–42	3.8	8.6	82.7	4.9	60	18.8	16.0
	42–70	1.0	1.6	96.4	1.0			
	70–95	0.8	0.4	91.8	7.0	100	22.6	22.3
Forest	0–5	3.2	13.0	72.1	11.6	20	17.0	7.1
	5–18	3.7	12.2	71.7	12.4			
	18–35	1.3	9.6	75.9	13.2			
	35–65	1.9	5.0	78.3	14.7	60	12.1	6.3
	65–70	8.9	8.0	66.2	16.9			
	70–100	7.3	3.1	71.8	17.7	100	9.2	6.4

TABLE 2 Forcing, calibration, and validation datasets with the spatial and temporal resolution of collection, with the location of data acquisition

Forcing datasets			
	Spatial resolution	**Temporal resolution**	**Data acquisition**
Precipitation (m/s)	N/A	15-min	Weather Station
Temperature (°C)	N/A	15-min	Weather Station
Wind speed (m/s)	N/A	15-min	Weather Station
Relative humidity (%)	N/A	15-min	Weather Station
Short wave radiation (W/m^2)	500 m	3 - hourly	ERA-interim (ERA, 2019)
Long wave radiation (W/m^2)	500 m	3 - hourly	ERA-interim (ERA, 2019)
δ^2H	N/A	Daily	Weather Station
$\delta^{18}O$	N/A	Daily	Weather Station
Calibration datasets			
Datasets	**Spatial resolution**	**Temporal resolution**	**Data acquisition**
Soil moisture (m^3/m^3) (3 probes in both grassland and Forest for each depth)	20 cm	15-min	UGT-SMT100
	60 cm	15-min	UGT-SMT100
	100 cm	15-min	UGT-SMT100
Transpiration (mm/day)*	Tree stand site	Hourly	Sap flow
Leaf area index (m^2/m^2)	500 m	4 day	MODIS (MCD15-v006, Terra; NASA (2019a))
Evapotranspiration (mm/day)	500 m	8 day	MODIS (MOD16-v006, Terra; NASA (2019b))
Latent heat (W/m^2)	500 m	8 day	MODIS (MOD16-v006, Terra; NASA (2019b))
Validation datasets			
Datasets	**Spatial resolution**	**Temporal resolution**	**Data acquisition**
Soil moisture (m^3/m^3)	20 cm	15-min	UGT-SMT100
	60 cm	15-min	UGT-SMT100
	100 cm	15-min	UGT-SMT100
LAI (m^2/m^2)	500 m	4 day	MODIS (MCD15-v006, Terra; NASA (2019a))
Evapotranspiration	500 m	8 day	MODIS (MCD15-v006, Terra; NASA (2019b))
Latent heat	500 m	8 day	MODIS (MCD15-v006, Terra; NASA (2019b))
Bulk soil water isotopes	2.5 cm	Monthly	Soil borehole
	7.5 cm		Soil borehole
	15 cm		Soil borehole
	25 cm		Soil borehole
	50 cm		Soil borehole
	90 cm		Soil borehole

*Used in the forest site only

transpiration is controlled by the canopy temperature and the canopy conductance using a Jarvis-type stomatal conductance model. The transpiration component considers the maximum plant responsiveness to saturated conditions ($g_{s,max,}$ Table 3) and the response to environmental stresses such as vapour pressure deficit ($g_{s,vpd}$, Table 3), light, temperature, and soil water availability. Root-uptake from each soil layer due to transpiration demand is determined by the proportion of roots in each soil layer and the water available in the soil layer (root distribution described in Kuppel, Tetzlaff, Maneta, & Soulsby, 2018b). The total transpiration is determined by the sum of the products of root-uptake and root proportion of all soil layers. The rooting zone function (proportion of roots in each soil layer) is an exponential function, and allocates the root distribution by the depth of each of the three soils layers. This formulation allows for a larger proportion of total root-uptake to occur from a soil layer with high water availability but lower rooting density than the other soil layers, albeit with a lower total transpiration rate. Canopy temperature and net radiation are used to estimate the surface energy balance, comprised of soil heat

TABLE 3 Priori parameter ranges of the soil and vegetation parameters used in calibration in the sand (forest site), loam (grassland site), and forest and grassland vegetation

Parameter		Calibration range	
Name			
Soil parameters	**Description**	**Sand (Forest)**	**Loam (grassland)**
ϕ	Soil porosity (m^3/m^3)	0.20–0.55	0.20–0.55
λ_{BC}	Brooks-Corey exponent parameter (–)	2.50–5.70	1.00–7.50
ψ_{ae}	Air-entry pressure head (m)	0.05–0.60	0.05–1.20
K_h	Saturated horizontal hydraulic conductivity (m/s)	1×10^{-5} - 0.75	1×10^{-8}–0.05
$K_v K_h$	Vertical to horizontal hydraulic conductivity ratio (–)	1×10^{-7} - 0.5	1×10^{-7}–0.40
L_g	Leakance out of groundwater (–)	1×10^{-4} - 10	1×10^{-3}–10
θ_r	Residual soil moisture (m^3/m^3)	0.01–0.02	0.01–0.10
K_{root}	Rooting exponential distribution factor (–)	0.10–50.0	0.10–50.0
D_{soil}	Soil depth (m)	0.70–3.0	0.70–2.50
Vegetation parameters			
		Forest	**Grassland**
$g_{s,max}$	Maximum stomatal conductance (m/s)	5×10^{-3}–3×10^{-2}	5×10^{-4}–5×10^{-2}
$g_{s,vpd}$	Stomatal conductance sensitivity factor due to vapour pressure deficit (–)	1×10^{-6}–1×10^{-3}	1×10^{-6}–1×10^{-3}
CWS_{max}	Maximum canopy interception storage per LAI (m)	1×10^{-4}–1.1×10^{-3}	1×10^{-5}–8×10^{-4}
Q_{we}	Quantum canopy efficiency ($gC^{2/}J/m$)	1×10^{-4}–1×10^{-7}	1×10^{-4}–1×10^{-7}
SLA	Specific leaf area (m^2/g)	0.01–0.10	0.01–0.10
LT_r	Mean leaf turnover rate (s^{-1})	1×10^{-9}–1×10^{-6}	1×10^{-9}–1×10^{-5}
$LT_{r,temp}$	Maximum leaf turnover rate due to cold stress (s^{-1})	1×10^{-9}–1×10^{-6}	1×10^{-9}–1×10^{-5}
$LT_{r,sat}$	Maximum leaf turnover rate due to water stress (s^{-1})	1×10^{-9}–1×10^{-6}	1×10^{-9}–1×10^{-5}

storage, latent heat of soil evaporation, and net radiation from the surface. Soil evaporation is then estimated as the maximum of the estimated latent heat and the total soil available water in layer 1 (the difference in porosity and residual soil moisture). EcH_2O-iso also comprises a vegetation dynamics module, which allows for the growth and decay of vegetation species. Growth and decay are simulated through the dynamics of leaves, stems, and roots, each of which influences the energy and water balance in the canopy and the soil (Maneta & Silverman, 2013). The growth and decay is regulated by the total estimated gross primary product, which is sensitive to the efficiency of the canopy to utilize water (Q_{we}, Table 3). Leaf growth dynamics are estimated as the difference between: the product of the allocation of net primary product to leaf growth and specific leaf area (SLA, Table 3), and the leaf turnover rate. Leaf turnover rate is governed by the mean turnover rate (LTr), temperature stress ($LT_{r,temp}$, Table 3) and water stress ($LT_{r,sat}$, Table 3). The dynamics of the leaf area index (LAI) largely regulates the net radiation reaching the ground and also regulates total stomatal surface that can transpire water, and the total water storage capacity of the canopy, among other effects. LAI seasonality therefore exerts a strong control on the dynamics of intercepted energy and water, which may especially drive the severity and recovery of droughts (Royer, Breshears, Zou, Cobb, & Kurc, 2010).

2.2.3 | EcH_2O-iso: Fractionation, water ages, and fractional water ages

Within EcH_2O-iso, the isotopic and water age module (Kuppel et al., 2018a) mixes and tracks incoming water (age and tracer composition) according to storage and accounting for each water layer. Complete mixing is conducted for each volume (layers 1, 2 and 3, and ponded water) on every time-step using a simplification of the complete mixing assumption (for both isotopes and water ages):

$$\delta_{new} = \frac{\delta_{old} \cdot (V_{new} - 0.5 \cdot Q_{in}) + (\delta_{in} \cdot Q_{in})}{V_{new} + 0.5 \cdot Q_{in}}, \quad (1)$$

where δ_{new} represents the new tracer or water age in storage, δ_{old} is the previous tracer or water age, Q_{in} is the incoming water flux to the layer, δ_{in} is the incoming tracer or water age, and V_{new} is a flux balance of incoming and outgoing water to each water layer ($V_{new} = 0.5 \cdot (V_{old} + Q_{in} + \max(V_{old} - Q_{out}, 0))$, V_{old} is the previous storage volume and Q_{out} is the water flux out of storage). As soil evaporation occurs only from the completely mixed soil layer 1, soil evaporation ages and isotopic compositions (non-vapour) are equivalent to those estimated for layer 1. Isotopic tracers are additionally influenced

by any isotopic fractionation using the Craig-Gordon model, adjusting the soil relative humidity based on Lee and Pielke (1992), isotopic turbulent factor based on Mathieu and Bariac (1996), and kinetic diffusion based on Vogt (1976) (Di/D = 0.9877 and 0.9859 for δ^2H and $\delta^{18}O$, respectively).

Fractional water ages were estimated in EcH_2O-iso to facilitate the evaluation of the distribution of water ages that form the mean water age. These fractional water ages were estimated on the calibrated parameter sets using artificial tracers in the isotopic module with isotopic fractionation was disabled. The model was run consecutively, starting with the first precipitation event, for each time-step that included precipitation. Each model run has a unique input time-series of the artificial tracer concentration of precipitation, with a unit concentration (value of one) on one precipitation event to assess the concentration changes through time. With an incoming unit concentration for only one event per simulation, the concentration represents the fraction of water in soil (or fluxes) of the precipitation event with no overlapping influence of subsequent events. For each run, the concentration in storage represents the fraction of stored water from the current unit concentration input. The summation of the concentration in a storage from all runs (over a long period) yields a soil water concentration with a value of one (all soil water is tracked to a precipitation event). For example, a catchment (time-step of 1 day) has 500 days of precipitation over a simulated 1,500 days. The calibrated model is run 500 times (all with 1,500 simulated days), once for each precipitation event. For example, if there is a precipitation event on June 1, the model is run by changing the artificial tracer input to one on June 1 and zero for all other days (one of 500 model runs). For this study, a spin-up period of 2-years prior to 2018 (2016–2018 from forcing datasets, Table 2) was used to initialize the fractional water ages for calibrated model parameters. Fractional water ages were assessed using the summation of soil water concentrations with moving averages of 7-day and for each 30-day increments up to 1 year to correspond to the isotopic measurement intervals (i.e., 7, 30, 60, 90, etc.). For each time-step, *t*, a backward window of the desired increment (e.g., 7-day) was used to identify the precipitation events within the window. At time *t*, the concentrations of each precipitation event within the backward window were summed to estimate the fraction of water in storage or flux (e.g., fraction of water younger than 7 days).

2.3 | Data acquisition for calibration and validation

2.3.1 | Model forcing (meteorological) datasets

The data available in the catchment for plot scale modelling is centred on combining existing weather stations operated by Deutscher Wetterdienst (DWD, 2019), a site implemented weather station at Hasenfelde (Figure 1a), and atmospheric reanalysis data (ERA-interim, ERA, 2019). As the Hasenfelde station was a new addition to the catchment, the total precipitation was compared to precipitation collected at Müncheberg, and only minor differences were recorded. Temperature, relative humidity, and wind speed (measured at 2 m above the surface) were also collected at Hasenfelde on 15-min sampling intervals and compared to the Müncheberg station with good correlation. This allowed the Müncheberg data to be used to complete the time-series at Hasenfelde between January–March 2018 (as the Hasenfelde weather station was installed in March 2018). As short and longwave downward radiation was unavailable at either the DWD station or at Hasenfelde, ERA-interim data were used as forcing data for the model. ERA-interim has been shown to be close to the measured values in the study area (Douinot et al., 2019). The three-hourly data of ERA-interim were interpolated to hourly using the p-chip interpolation method (Fritsch & Carlson, 1980) which prevents negative radiation (shortwave specific) and gap-fills the dataset appropriate to the model resolution. Daily isotopes in precipitation were collected at Hasenfelde beginning in June 2018 and analysed for δ^2H and $\delta^{18}O$ with an off-axis Integrated Cavity Output Spectroscopy (OA-ICOS) (Triple Water-Vapour Isotope Analyser TWIA-45-EP, Model#: 912–0032-000 Los Gatos Research, Inc., USA) in liquid analysed mode. Line-conditioned excess (lc-excess) (Landwehr & Coplen, 2006) is a useful measure for identifying periods of significant evaporation, notably when lc-excess is less than 0. Lc-excess was estimated for measured (and simulated) soil isotopes using the slope and intercept of the local meteoric water (7.46 and 5.66 for the slope (*a*) and intercept (*b*), respectively) ($lc-excess = \delta^2H - a \times \delta^{18}O - b$).

2.3.2 | Calibration and validation datasets

Soil moisture was measured at the grassland and forest plots in three locations and at three depths (20, 60, and 100 cm) with UGT-SMT100 soil moisture probes (UGT, 2019) on 15-min intervals. The three locations provide an indication of the soil heterogeneity of each site. Sap flow measurements were conducted on 12 trees in the forest site using 2–4 thermal dissipation-based sap flow sensors (TDP probes, *Dynamix Inc*., Houston, TX), radially installed in each tree. To represent the tree frequency in the plot, nine TDP probes were installed in *Quercus robur*, and one probe in each *Quercus rubra*, *Corylus avellana*, and *Pinus sylvestris*. Temperature data were logged each hour by a CR1000 datalogger (Campbell Scientific, USA) with sap flux density and sap flow estimated in the same way as Komatsu et al. (2012). Sap flow estimations were averaged for each tree and for the plot weighted using the sapwood area. To qualitatively examine the energy balance, vegetation growth, and evapotranspiration, MODIS datasets of leaf area index (LAI), latent heat (LE), and evapotranspiration (ET) were collected and processed for the pixel containing both sites (500 m grid size). MODIS datasets were quality checked and evaluated with the QC flags, where data with large uncertainty or high unexplained temporal variability were not considered for calibration or validation. Datasets for the LAI were available on 4-day average time-step, while LE and ET were available only on eight-day average time-steps (NASA, 2019a, 2019b). Soil water isotopes were collected monthly, beginning in October 2018. Soil samples were collected (with two replicates) at average depths of 2.5, 7.5, 15, 25, 50, and

90 cm at each site (Kleine, Tetzlaff, Smith, Wang, & Soulsby, 2020). Soil samples were analysed for stable isotopes δ^2H and $\delta^{18}O$ by equilibrating dry air added to the sealed soil bag over 48 hours and analysing the vapour isotopic composition with Picarro Gas Analyser (L2130-*i*) (Wassenaar, Hendry, Chostner, & Lis, 2008). Corrections of the isotopic compositions of soil water for organic gas matrix changes were made after isotopic analysis using the method described in Gralher, Herbstritt, Weiler, Wassenaar, and Stumpp (2018).

2.4 | Standardized precipitation index (SPI) and lag analysis

To evaluate the stress of limited precipitation on the soils and vegetation, the standardized precipitation index (SPI) was assessed using the daily precipitation from 1951–2018, the total duration of the precipitation record at the closest long-term climate station. The SPI was used to best provide an indication of extreme dryness conditions (McKee, Doesken, & Kleist, 1993). To evaluate a stepwise comparison of the precipitation index, the estimation of SPI was conducted for each Julian day by using a moving sum with an equal time-step before each Julian day. The SPI was assessed with four different moving window sizes (backwards window only), 30, and 60, 180, and 365-day, corresponding to 1 month, 2-month, half-year, and 1-year SPI. The windows were used to estimate the climatological means to compare different Julian days. The lengths of the backward windows provide different information regarding the drought stress, where the smaller windows (30 and 60-day) suggest immediate stress while the larger windows (180 and 365-day) suggest a long-term and more severe stress. The SPI was estimated by fitting a gamma distribution to the Julian day precipitation amount for each moving window, with an estimated t-statistic and percentile for the Julian day of each year. Negative t-statistics indicate lower than normal precipitation of the same historical window. The beginning and end of the drought for each respective SPI were determined by the t-statistic, where a t-statistic of −1 on a 30-day window was used to characterize the drought. For our study, the primary drought period was between May 26, 2018, and September 30, 2018, after which the SPI increased above −1 for an extended period (not driven by a single event). The end of the recovery period was similarly characterized by a decrease of the SPI below −1 (April 8, 2019, beginning of another low precipitation period).

Temporal lags in the soil moisture time-series data were estimated using the lag in cross-correlation (Stoica & Moses, 2005). The lag in cross-correlation between soil moisture values in different soil layers is output with the greatest significance (with conditions that $p < .05$).

2.5 | Model calibration, validation, and evaluation

2.5.1 | Performance metrics

The model was evaluated using a variety of performance metrics, used to best evaluate the temporal variability of particular data sets. The primary performance metrics used to assess the calibration and validation of the model were the mean absolute error (MAE), Kling-Gupta efficiency (KGE) (Kling, Fuchs, & Paulin, 2012), and Nash-Sutcliffe efficiency (NSE) (Nash & Sutcliffe, 1970). The MAE ($MAE = \left(\sum_{i=1}^{n}|Sim_i - Meas_i|\right)/n$) was used to measure the average simulation difference to a dataset when the measured variability of soil moisture (%) is low (ratio of variance to mean < 1) and for the MODIS datasets. The performance of the model against MODIS datasets were evaluated only using the MAE due to the uncertainty of variability, the relatively large grid encompassing multiple vegetation and soil types, and the larger time-step of the MODIS datasets The KGE and NSE were used simultaneously to optimize the simulations to soil moisture (%) datasets with significant temporal variability. The KGE ($KGE = 1 - \sqrt{(1-r)^2 + (1-\alpha)^2 + (1-\beta)^2}$) provides a balance of the mean (ratio of means, $\beta = \mu_{Sim}/\mu_{Meas}$), standard deviation (ratio of standard deviations, $\alpha = \left(\frac{\sigma_{Sim}}{\mu_{Sim}}\right)/\left(\frac{\sigma_{Meas}}{\mu_{Meas}}\right)$), and correlation coefficient (Pearson correlation coefficient, *r*), while the NSE ($NSE = 1 - \frac{\sum(-Meas)^2}{\sum(Meas-\mu_{Meas})^2}$) provides a ratio of the variance of the simulation to the measured data. Initial testing of the model revealed that NSE or KGE values below 0.4 did not show adequate simulations, so a minimum acceptable NSE and KGE of 0.4 was set for the simulations. To ensure a minimum performance metric of NSE and KGE of 0.4, values below the 0.4 thresholds were given values of 0. These methods (or their subsequent components, e.g., *r*) have been used to compare model simulations of soil moisture to measured soil moisture and model simulations of LAI, LE and ET to MODIS images (Fensholt, Sandholt, & Rasmussen, 2004; Hwang et al., 2008; Trombetta, Iacobellis, Tarantino, & Gentile, 2016).

2.5.2 | Calibration

The model was set up independently for the grassland and forest sites using the fenced (controlled) area of each site to average the measured conditions, with a boundary of a 10 m × 10 m grid square. The model was set-up with an hourly time-step and calibrated between June first, 2018, to December 31, 2018, following a spin-up period from January 1, 2018 to May 31, 2018, using stepwise multicriteria calibration. Initial conditions of soil moisture and soil isotopes were set using the average of measured soil moisture of the following January (2019). The model exhibited limited differences in soil moisture or soil isotopes with a spin-up period longer than 6 months. The initial conditions of water age in each soil layer were set by running the model for 3 years (twice the original simulation time) for each parameter set to ensure that no long-term increasing trend was present. The stepwise calibration was conducted in two stages: water and energy balance calibration (soil moisture, ET, LE, and transpiration in the forest, and soil moisture, ET, and LE in the grassland), and vegetation growth calibration (LAI at both sites) (soil and vegetation parameters shown in Table 3, posterior parameter ranges shown in Appendix A). Multicriteria calibration was conducted for each stepwise calibration. In both sites, soil moisture in layers 1 and 2 was calibrated using KGE and NSE (based on the variability criteria), while

layer 3 was calibrated using MAE because of a lack of variability. The LAI, LE, transpiration (transpiration in the forest site only) and ET were all calibrated using KGE and NSE. Both calibration steps included 100,000 Latin Hypercube Sampling calibration parameters sets (200,000 total calibration parameter sets). Parameter sets were calibrated by normalizing each performance metric between 1 (best) and 0 (worst). For each simulation, the minimum of all performance metrics was used to rank the simulation performance and retain the 100 "best" simulations.

2.5.3 | Validation

Model validation was conducted between January 1, 2019 and May 31, 2019 following the beginning of the wet-up period (December 2018), including the soil moisture recovery period and the subsequent drawdown in the following spring (April–May 2019). Similar to the calibration period, the validation period was assessed using soil moisture, LAI, LE, and ET; however, transpiration in the forest site was not available for the validation period in the forest. Soil water isotopes (δ^2H, and lc-excess) were used to informally validate soil water mixing and soil evaporation processes through the whole simulation period (calibration and validation period inclusive). The MAE of the δ^2H and lc-excess were calculated for each soil layer (no maximum criteria was set for rejection). As there were relatively few soil isotope samples available during the calibration period, the whole data set were separated into each soil layer (layer 1:0–15 cm, layer 2:15–50 cm, and layer 3: >50 cm) and evaluated as validation of the models' longer-scale internal simulation dynamics.

2.5.4 | Evaluation of soil and vegetation sensitivity to fluxes and water ages

To test the principal factors in the quantity and responsiveness of storages, fluxes, and water ages, different combinations of soil (sandy loam (grassland) and loamy sand (forest)) and vegetation (grass and forest) were evaluated against the calibrated simulations (referred to as the baseline conditions). From calibration there were 100 "best" parameter sets pertaining to vegetation and soil. New uncalibrated combinations of soil and vegetation parameter sets (e.g., sandy loam and forest) were randomly designated from the calibrated vegetation and soil parameter sets. To remove bias of a single combination of soil and vegetation parameter sets, 100 random combinations of vegetation and soil parameters were selected. One hundred random combinations were chosen for direct comparison to the 100 "best" baseline conditions.

The effects of changing the soil under the grass (sandy loam to loamy sand) and vegetation on sandy loam (grass to forest) was evaluated using the 100 "best" calibrated simulations at the grassland site as baseline conditions. Similarly, the effects of changing the soil under forests (loamy sand to sandy loam) and vegetation on loamy sand (forest to grass) were assessed using the forest site as baseline conditions. The change was assessed as the absolute percent change on each time-step ($\%\text{Change} = \left(\sum_{t=1}^{ts}|C(t)-S(t)|\right)/ts/\sum_{t=1}^{ts}C(t)\times 100$), where $C(t)$ is the calibrated simulation baseline, $S(t)$ is the simulation with changed soil (or vegetation) parameters, and ts is the number of time-steps. With parameters for each soil and vegetation type, the significance of the change from the baseline in storage, flux or water age was assessed using the Wilcox-rank sum test, which does not assume a normal distribution (Mann & Whitney, 1947). To better understand whether the change in soil or vegetation is more significant for storage, flux, and water age, the difference in percent change for changing soil and changing vegetation was also assessed with the Wilcox-rank sum test. The percent change and significance levels were estimated for the whole time-series and the drought and recovery periods.

3 | RESULTS

3.1 | Effect of drought and recovery on ecohydrologic fluxes

Precipitation during the summer of 2018 was very low with respect to the long-term historical record (1951–present; DWD, 2019), with only one large event during the summer of 2018 (Figure 2a). Similarly, the 30 and 60-day moving SPI during the summer were below −1 (one standard deviation below the mean, Figure 2b) for the majority of the summer. Total precipitation increased towards the end of the year (December 2018) with SPI (30 and 60-day) at long-term average values (SPI = 0). In addition to the reduced precipitation, the drought of 2018 was accompanied by higher than average air temperature (Figure 2c) and lower than average relative humidity (Figure 2d). Soil moisture in the forest (Figure 2e) and grassland (Figure 2f) reflect the limited precipitation input to the catchment. Soil moisture in the forest responds faster to precipitation than the grassland. However, soil moisture at the grassland site is consistently higher than the equivalent depth in the forest (Figure 2e,f). Both sites show delayed response in soil moisture with depth (lag in cross-correlation, Stoica & Moses, 2005), in the forests the soil moisture at 60 cm shows an 18-day lag (p-value <.05), and 100 cm shows a 42-day lag (p-value <.05) from the 20 cm soil moisture. In the grassland, there is a 28-day lag (p-value <.05) from 20 to 60 cm; however, there is only a very small response in soil moisture at 100 cm with a 53-day lag only discernible with normalized soil moisture (p-value >.05 on non-normalized data, p-value <.05 on normalized data).

The calibration period produced reasonable results for each measured soil moisture where the most variable measured soil moisture (20 and 60 cm) was adequately captured by the soil layer 1 and layer 2 respectively (Figure 3a,d). While soil moisture in layer 2 did not yield as much variability as the mean measured soil moisture (Figure 3b,e), simulations were within the measurement bounds and yielded a response similar to the lower measured soil moisture bound and in the forest site, captured the observed increase during the winter (2018–2019). Simulated soil moisture in layer 3 did not show large

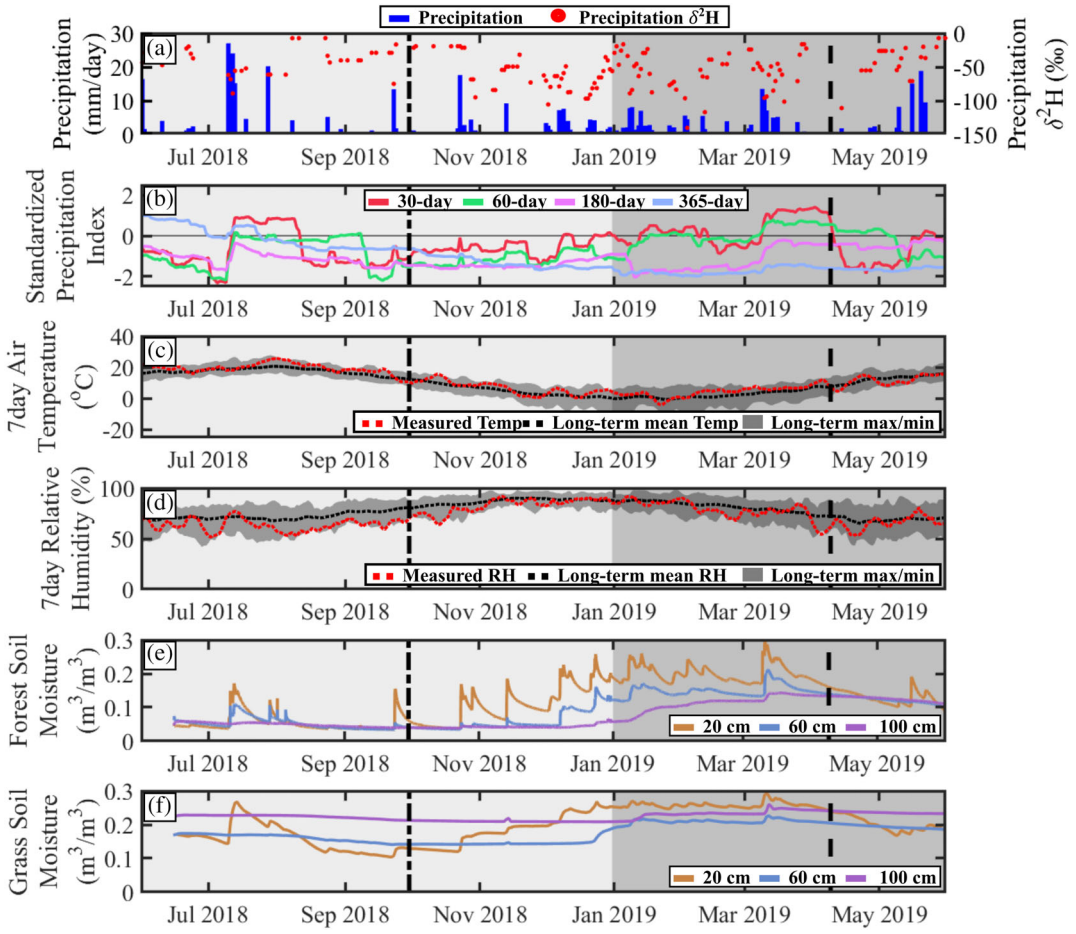

FIGURE 2 (a) Daily precipitation and isotopic composition (δ^2H)in precipitation (b) moving average standardized precipitation of 30, 60, 180, and 365-day moving average trends, (c) 7-day average air temperature at 2 m, (d) 7-day average relative humidity at 2 m, (e) mean daily soil moisture in the forest at 20, 60, and 100 cm, and (f) mean daily soil moisture in the grassland at 20, 60, and 100 cm. For all plots, the vertical lines indicate the end of the drought and end of the recovery period

variability at either site (Figure 3c,f); however, simulations at both sites showed a modest increase in soil moisture during the winter with some over-estimation of soil moisture during the drought (Figure 3c). The limited drawdown of soil moisture in layer 3 is likely due to the deeper calibrated soil layer 3 (Appendix A) than the measurement depth (100 cm), with a deeper soil stabilizing the total water storage in layer 3. The validation period (January–June 2019) did not perform as well, primarily due to moderate under-estimation of soil moisture in layer 1 at both sites in March 2019 (Figure 3a,d). This period coincides with a higher than normal precipitation (30 and 60-day SPI > 1, Figure 2b) during the wetter winter period. However, with the upper bounds of the simulations capturing the mean measured soil moisture conditions during this period, the model adequately captured high precipitation in the wet winter and the drought. Soil parameter ranges were most identifiable for soils in the grassland for the porosity, leakance, root distribution parameter and soil depth (see Appendix A, decrease in interquartile range). Soil parameters were not as identifiable in the forest (porosity and Brooks-Corey parameter, see Appendix A). Some of the limitations in identifiability are likely due to the inter-relationship of model parameters. Vegetation parameters were more identifiable for both sites, with canopy storage, canopy efficiency, and leaf turnover rates showing notable decreases from the prior parameter ranges (Appendix A).

The simulated energy balance (LE) and "green" water fluxes (ET) were satisfactory compared to measured datasets (calibrated simulations of LAI for both sites and transpiration in the forest shown in Appendix B), with simulated energy balance components (e.g., latent heat, Figure 4a,e) showing a similar magnitude and dynamics to MODIS datasets. There was some under-estimation of ET in the forest compared to the MODIS data, though this was primarily limited to the most severe parts of the drought (Figures 3a and 4b). The larger variability of simulated ET compared to MODIS ET was mainly due to the large measured variability of sap flow, which the simulations were able to reproduce in the transpiration flux (Appendix B). In the summer drought, soil evaporation and groundwater recharge at the forest site (Figure 4c,d) were negligible. Soil evaporation was generally low in the forest, accounting for 10 ± 4% of total ET between January 2018 and May 2019. Soil evaporation in the forest rebounded following the winter recovery period and prior to significant leaf growth (March–May 2019) when soil evaporation was not in competition

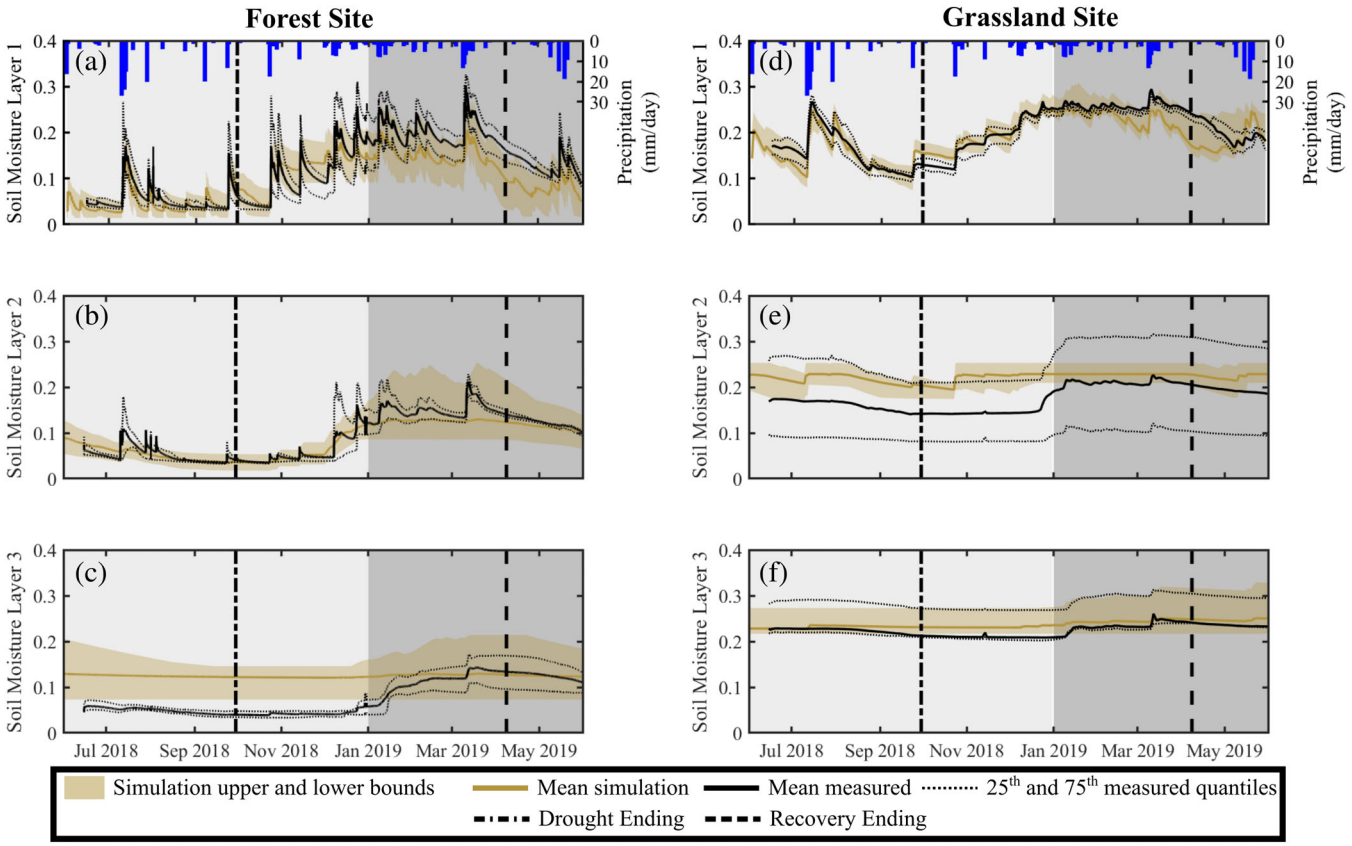

FIGURE 3 Calibration (light grey) and validation (dark grey) simulations of soil moisture of each soil layer in the forest plot (a–c) and grassland plot (d–f)

with root-uptake (Figure 4b). In the forest, groundwater recharge predominantly occurred during the winter, beginning mid-December and receding in spring (April and May 2019, Figure 4d). Despite the short recharge period, the groundwater recharge accounted for 27 ± 8% of the total precipitation to the forest site.

The latent heat estimated in the grassland was moderately less than the MODIS grid data; however, the MODIS data did not account for shading of the nearby forest and the relatively large grid (500 m × 500 m) primarily contained forested areas. As with the forest site, the ET was under-estimated in the grassland site relative to the MODIS grid. Similar to the latent heat estimation, the MODIS grid was predominantly forest so lower ET was anticipated. Soil evaporation and groundwater recharge in the grassland site were additionally less affected during the drought than the soil evaporation and groundwater recharge at the forest site (Figure 4g,h). Soil evaporation in the drought corresponded to the soil moisture conditions in layer 1 (Figures 3d and 4g), with higher fluxes following the large rainfall event in July. As with the forest, the soil evaporation in the grassland rebounded in the spring of 2019. Although the wet and mild winter (2018–2019) would likely result in more soil evaporation than a typical winter (freezing temperatures), the estimated total soil evaporation flux is likely high for the 2019 spring. Soil evaporation accounted for 48 ± 11% of total ET within the study period (January 2018 to May 2019). Groundwater recharge occurred throughout the year in the grassland site (Figure 4h) with higher recharge rates only during the large precipitation events (July 2018, January 2019, March 2019, and May 2019). Due to the relatively constant recharge rate throughout the year, groundwater recharge accounted for 33 ± 9% of the total precipitation in the grassland site.

The general sensitivity of storages and fluxes is temporally insensitive to the drought or recovery periods (Appendix C). The ET and transpiration were consistent throughout the simulation, showing highest sensitivity to vegetation type, while soil moisture in layers 2 and 3 were consistently most sensitive to the soil type (Table C1). Soil evaporation, groundwater recharge, and soil layer 1 exhibited some temporal differences in the sensitivity, though changes in the sensitivity were inconsistent between the sites with the sensitivity against the forest baseline conditions showing the greatest temporal differences (Table C1).

3.2 | Influence of drought and rewetting on soil water isotopes and ages

Simulated soil water isotopes reflect the dynamics of the measured bulk soil water isotopes in each soil layer, despite not being used in calibration (Figure 5b–d, f–h). In the forest, δ^2H simulations captured the higher dynamics of the measured δ^2H in layer 1 (Figure 5b,

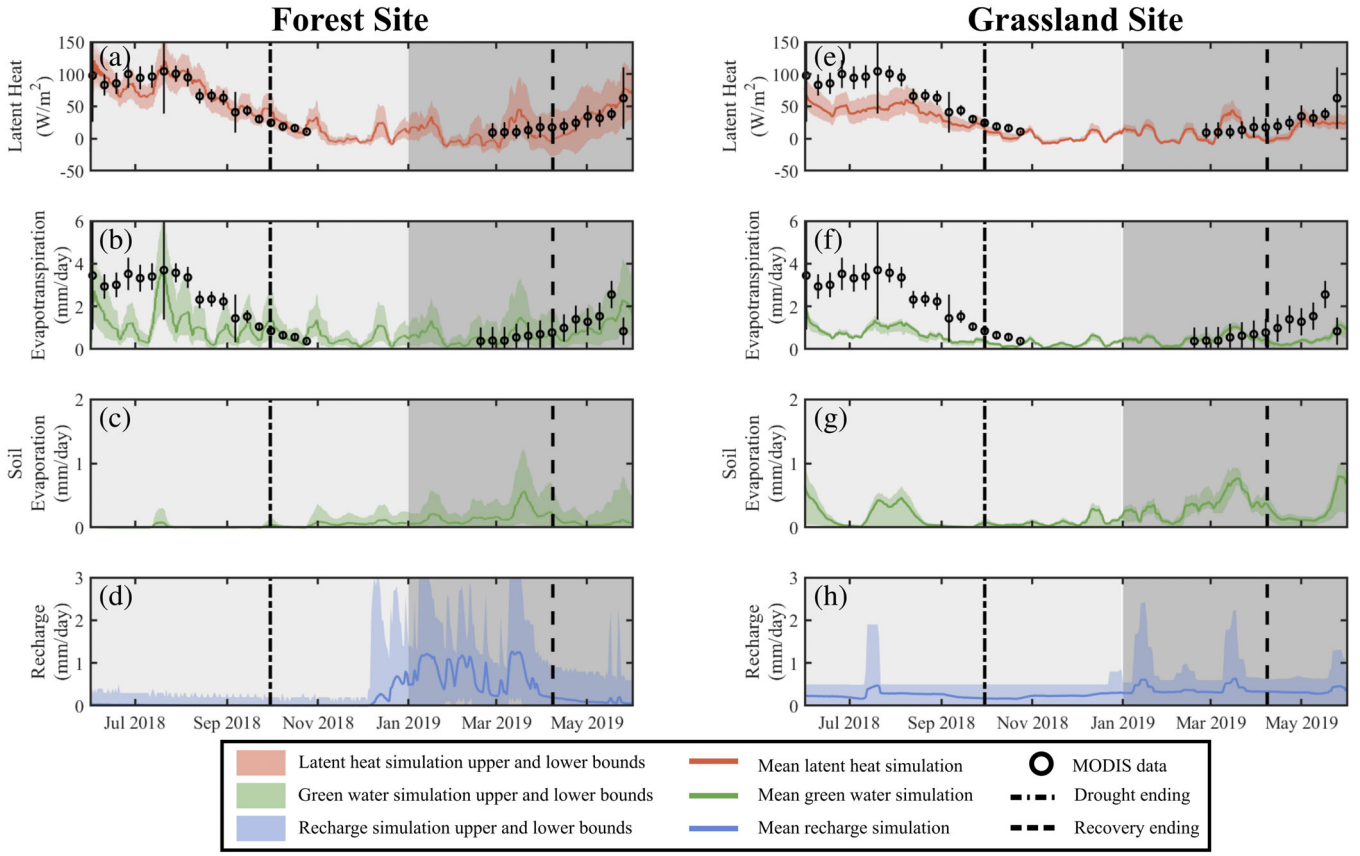

FIGURE 4 Calibration (light grey) and validation (dark grey) of the latent heat, green water fluxes (evapotranspiration, and soil evaporation) and blue water fluxes (groundwater recharge) in the forest site (a–d) and grassland site (e–h), respectively

measured and simulated temporal standard deviation, 13.1 and 14.7‰, respectively) relative to the lower soil layers (uncalibrated MAE in layer 1 for δ^2H and lc-excess was 9.6 and 4.9‰, respectively). There were short periods of under-enrichment of simulated δ^2H in layer 1 relative to the measured isotopic compositions. The depleted simulated δ^2H and higher lc-excess than measured (October–December 2018, Figure 5b) coincide with low soil evaporation in the forest (Figure 4c) (uncalibrated MAE in layer 1 for δ^2H and lc-excess without summer samples was 5.5 and 26 ‰, respectively). Variability in δ^2H was more damped in layer 2 than layer 1 (Figure 5c, measured and simulated temporal standard deviation, 6.6 and 5.5‰, respectively), and damped further in layer 3 (Figure 5d, measured and simulated temporal standard deviation, 1.4 and 3.8‰, respectively). The δ^2H and lc-excess were both reasonably captured with an average MAE of 5.3 and 1.2‰ for δ2H and lc-excess, respectively for layers 2 and 3. A similar effect of under-enrichment in layer 2 in the forest (Figure 5c) was likely due to the lagged effect of the depleted soil δ^2H and higher lc-excess from layer 1. In the grassland, higher evaporation and evaporative fractionation resulted in a more enriched isotopic composition (lower lc-excess) in layer 1 than the forest at the end of 2018 (mean lc-excess was −10.5 and −6 ‰ in the grass and forest, respectively). Unlike the forest site, the grassland simulations experienced some over-enrichment, primarily during the winter months (uncalibrated MAE in layer 1 for δ^2H and lc-excess was 13.7 and 3.1‰, respectively). Simulations additionally captured the variability of δ^2H in the grassland shallow soils (layer 1) (Figure 5f, measured and simulated temporal standard deviation, 12.5 and 9.3‰, respectively). Similar to the forest site, grassland isotopic simulations improved with depth (average MAE of 4.3 and 1.3‰ for δ^2H and lc-excess, respectively for layers 2 and 3), and were slightly better than the deeper soil simulations in the forest. Simulations and measurements in the forest also show damping occurred in layers 2 and 3 (Figure 5g,h) with lower variability of both δ^2H and lc-excess in layer 2 than layer 1 (Figure 5g, measured and simulated temporal standard deviation, 4.7 and 3.7‰, respectively). Isotopic variability was particularly reduced in grassland layer 3 (Figure 5h, measured and simulated temporal standard deviation, 3.8 and 0.8‰, respectively); however, the relatively low simulated variability and higher measurement variability suggests that some of the measured variability may be due to spatial differences.

Simulated soil water ages for each soil layer were distinctly different for both the forest and grassland sites. Soil water in layer 1 in the forest was the youngest and most dynamic water on average (Figure 5a) but exhibited slightly greater changes in the mean age during the drought compared to the long-term average or recovery period (Table 4). The decrease in water age in layer 1 in the forest during the drought was likely due to the low soil moisture accentuating the influence of new precipitation inputs (age of 0 days). The water ages in the grassland were consistently older than the forest, as well

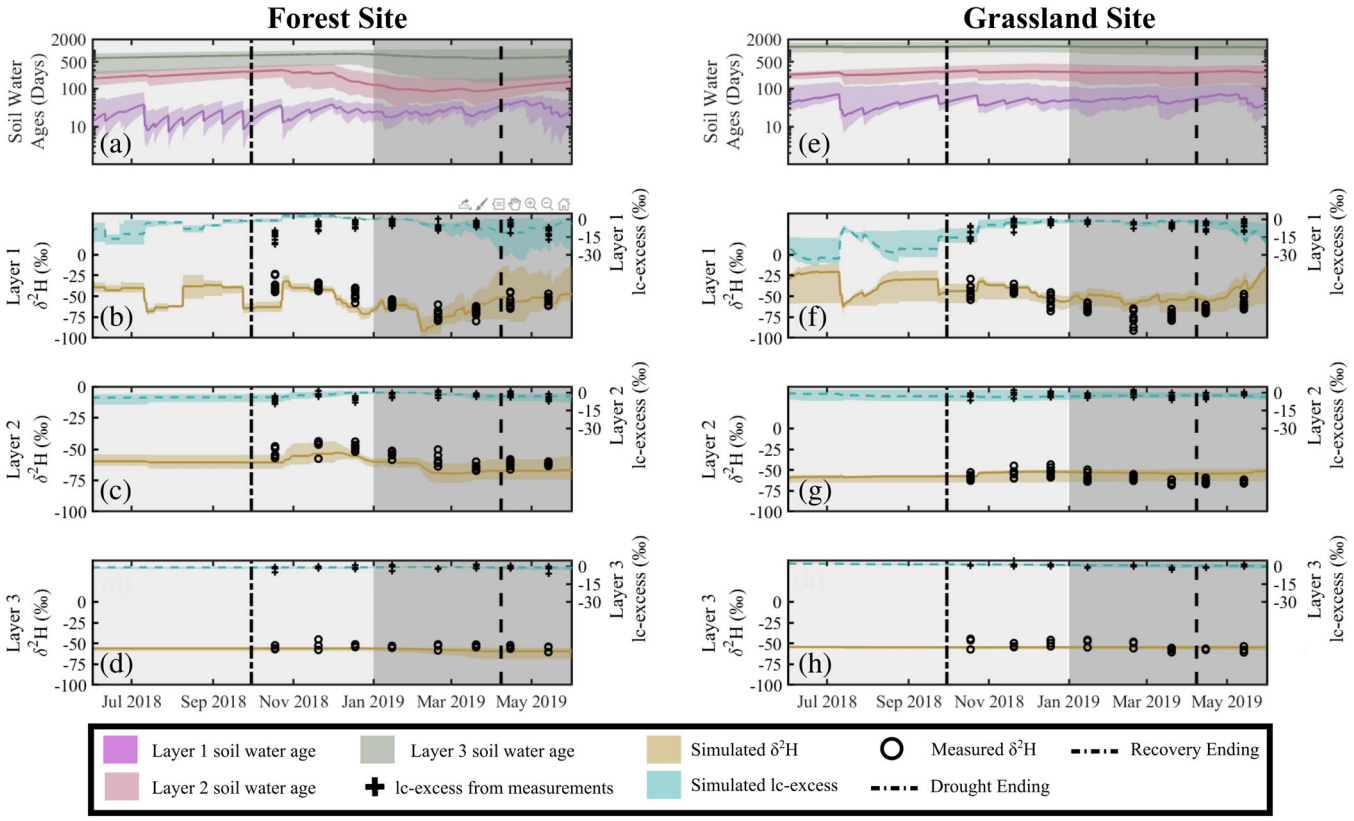

FIGURE 5 Simulations in the calibration (light grey) and validation (dark grey) periods of soil water ages (a and e) and soil water isotopes δ^2H and corresponding lc-excess (b–d and f–h) in the forest and grassland site respectively

TABLE 4 Long-term, drought (May 26, 2018–Sept 30, 2018), and Recovery (Oct 1, 2018–April 8, 2018) period water ages in each soil layer in the grassland and forest sites

		Grassland	Forest
Layer 1 age (days)	Long-term	48 ± 11	24 ± 5
	Drought	51 ± 10	20 ± 7
	Recovery	49 ± 11	24 ± 5
Layer 2 age (days)	Long-term	264 ± 69	180 ± 42
	Drought	254 ± 47	234 ± 38
	Recovery	271 ± 70	169 ± 49
Layer 3 age (days)	Long-term	1,252 ± 336	707 ± 150
	Drought	1,256 ± 299	690 ± 122
	Recovery	1,260 ± 336	742 ± 152

as less variable throughout the year (Figure 5e). Water ages in layer 1 were almost twice as old as the forest (Table 4), with more comparable water ages in layer 2. However, layer 2 in the grassland showed limited temporal variability (Figure 5e).

Throughout the year, soil water at the forest site in layer 1 was dominated by water younger than 30 days (Figure 6a, Table 5), with a notable and seemingly paradoxical increase in the younger fraction of 30 and 60 day water during the drought (Table 5). However, the fractional water ages in layer 1 are very flashy in response to new water inputs, with high peaks of fractional water age younger than 7 days following precipitation events. Despite this, the contribution of water younger than 30 and 60 days during the drought does not return to pre-drought fractions until the post-recovery period (Table 5). Unlike layer 1, during the drought layers 2 and 3 in the forest showed decreasing fractions of water in the younger than 30, 60 and 180-day fractions (Figure 6b,c and Table 5). Layer 3 in the forest additionally showed decreasing fractions of 365-day water during the recovery period, likely lagged from the drought as younger waters percolated to depth (Table 5). In both layers, the fractions of 30, 60, and 180-day water returned to pre-drought conditions either in the recovery or post-recovery period. With soil evaporation occurring only from layer 1, the fractional water ages of evaporation in the forest are the same as to the fractional ages in layer 1 (Figure 6a). Rooting depths spanning all three soil layers in the forest results in a unique temporal change in the fractional water used in transpiration. In the driest periods of the drought, transpiration has a higher fraction of old water (Figure 6d,e,g older than 180 days) than after the drought (Table 5). In the post-recovery period, (recovery period has limited transpiration), transpiration again is fed much more by younger water fractions (Table 5).

The grassland site has a substantially higher fraction of older water in layer 1 compared to the forest site (Figure 6a,e), with the older water still evident in the grassland site even during the wetter periods (pre-drought, recovery, and post-drought). During the drought, fractions of

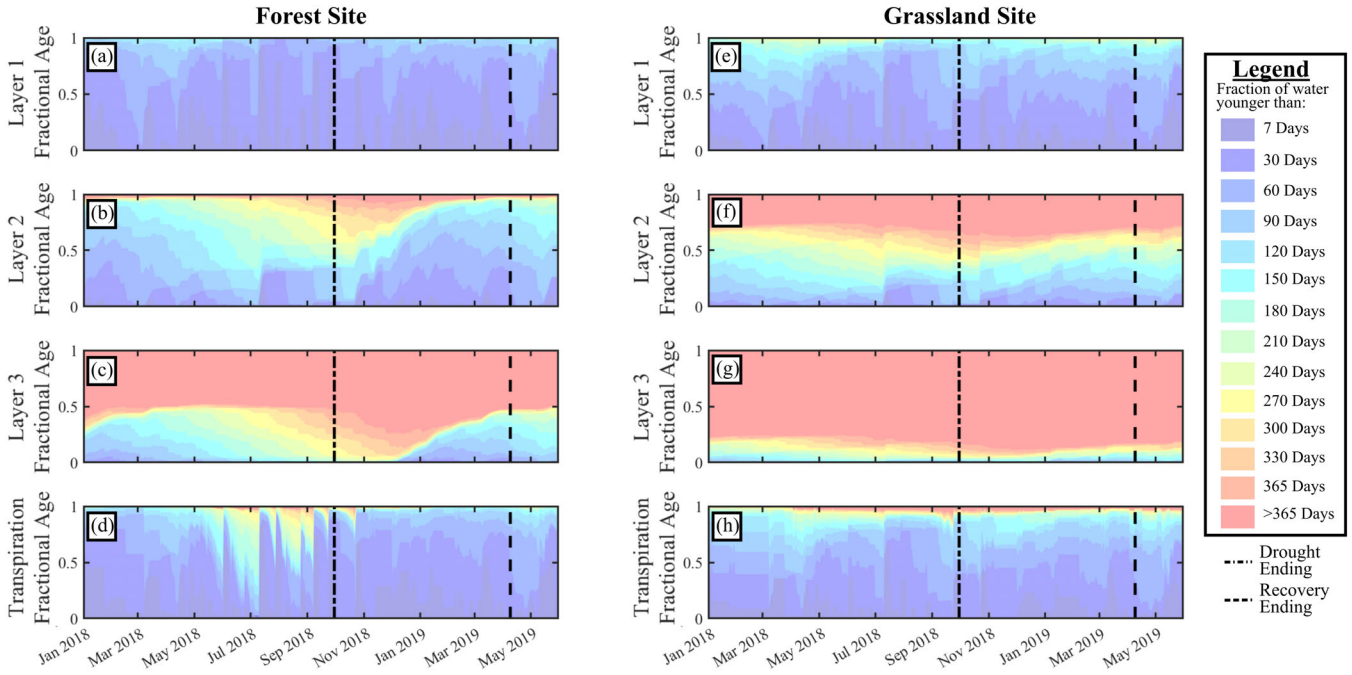

FIGURE 6 Forest and grassland site fractional water ages of water in storage younger than a certain age (7-day, and 30-day increments up to 1 year). Water older than 1 year was aggregated into a single fraction, water >365 days. Fractional water ages are shown for layer 1 (a and e), layer 2 (b and f), layer 3 (c and g), and transpiration (d and h)

TABLE 5 Average fractions (standard deviation) of water ages younger than 30, 60, 180, and 365 days at the Forest and Grassland sites in the pre-drought (Pre D, Jan 1, 2018–May 25, 2018), drought (D, May 26, 2018–Sept 30, 2018), recovery (R, Oct 1, 2018–Apr 8, 2019), and post-recovery (post R, Apr 9, 2019–May 31, 2019) period

		Forest site				Grassland site			
		30 days	60 days	180 days	365 days	30 days	60 days	180 days	365 days
Layer 1	Pre D	0.61 ± 0.07	0.85 ± 0.06	1.00 ± 0.00	1.00 ± 0.00	0.39 ± 0.09	0.59 ± 0.11	0.96 ± 0.04	1.00 ± 0.00
	D	0.74 ± 0.10	0.96 ± 0.03	1.00 ± 0.00	1.00 ± 0.00	0.39 ± 0.07	0.76 ± 0.08	0.97 ± 0.04	1.00 ± 0.01
	R	0.70 ± 0.07	0.92 ± 0.04	1.00 ± 0.00	1.00 ± 0.00	0.46 ± 0.10	0.69 ± 0.10	0.98 ± 0.03	1.00 ± 0.01
	Post R	0.56 ± 0.06	0.86 ± 0.05	1.00 ± 0.00	1.00 ± 0.00	0.41 ± 0.06	0.68 ± 0.08	0.96 ± 0.03	1.00 ± 0.01
Layer 2	Pre D	0.15 ± 0.06	0.36 ± 0.10	0.92 ± 0.05	0.98 ± 0.02	0.03 ± 0.02	0.09 ± 0.07	0.46 ± 0.22	0.73 ± 0.22
	D	0.02 ± 0.02	0.15 ± 0.09	0.60 ± 0.15	0.98 ± 0.02	0.02 ± 0.01	0.10 ± 0.05	0.34 ± 0.15	0.70 ± 0.20
	R	0.21 ± 0.06	0.42 ± 0.09	0.75 ± 0.09	0.95 ± 0.04	0.05 ± 0.04	0.13 ± 0.08	0.43 ± 0.15	0.65 ± 0.18
	Post R	0.12 ± 0.05	0.33 ± 0.10	0.92 ± 0.05	0.98 ± 0.02	0.04 ± 0.03	0.10 ± 0.06	0.45 ± 0.22	0.70 ± 0.18
Layer 3	Pre D	0.01 ± 0.01	0.06 ± 0.05	0.37 ± 0.19	0.49 ± 0.22	0.00 ± 0.00	0.00 ± 0.01	0.08 ± 0.08	0.24 ± 0.20
	D	0.00 ± 0.00	0.00 ± 0.01	0.11 ± 0.09	0.50 ± 0.21	0.00 ± 0.00	0.01 ± 0.00	0.03 ± 0.03	0.20 ± 0.17
	R	0.02 ± 0.01	0.06 ± 0.04	0.16 ± 0.11	0.35 ± 0.20	0.00 ± 0.00	0.01 ± 0.01	0.05 ± 0.03	0.14 ± 0.10
	Post R	0.01 ± 0.01	0.04 ± 0.04	0.39 ± 0.18	0.48 ± 0.21	0.00 ± 0.00	0.00 ± 0.01	0.07 ± 0.07	0.18 ± 0.12
Transpiration	Pre D	0.56 ± 0.08	0.73 ± 0.08	0.98 ± 0.02	1.00 ± 0.01	0.41 ± 0.05	0.58 ± 0.06	0.90 ± 0.05	0.98 ± 0.02
	D	0.39 ± 0.11	0.54 ± 0.13	0.80 ± 0.09	0.98 ± 0.01	0.34 ± 0.07	0.68 ± 0.09	0.89 ± 0.06	0.96 ± 0.03
	R	0.65 ± 0.07	0.87 ± 0.05	0.97 ± 0.02	0.99 ± 0.00	0.42 ± 0.03	0.62 ± 0.03	0.93 ± 0.01	0.97 ± 0.01
	Post R	0.48 ± 0.06	0.77 ± 0.07	0.98 ± 0.01	1.00 ± 0.00	0.36 ± 0.05	0.62 ± 0.06	0.92 ± 0.04	0.97 ± 0.02

water younger than 60 days increase in the grassland site layer 1 (0.59–0.76, Table 5); however, the fractions of water younger than 60 days did not decrease to pre-drought conditions within the simulation period (0.68 following post-recovery). Similar to the forest site, young water fractions in layer 2 and 3 in the grassland decreased during the drought, for 30, 60, and 180-day fractions in layer 2, and 180-day fractions in layer 3 (Figure 6f,g). These fractions rebounded during the recovery period. However, decreases in the water age fraction of

365 days in layers 2 and 3 were delayed until the recovery period, with only the fraction in layer 2 rebounding by the end of the post-recovery period. With soil evaporation occurring only from layer 1, the fractional water of soil evaporation in the grassland site was equivalent to that in layer 1. Shallower rooting depths in the grassland resulted in higher young water fractions in transpiration throughout the year and were similar to the age fraction in layer 1. However, during the drought, the transpiration fraction of water younger than 30 days decreased rather than increased, more closely reflecting layer 2 than layer 1 (Figure 6h).

The sensitivity of the model water age simulations to changes in soil and vegetation show temporal variability from during the drought to the recovery following the drought. At both sites, the change in vegetation was the most significant ($p < .01$, symbol b) for estimating the transpiration water age, with larger influences in the transpiration water age during the recovery period. During the drought, layer 1 water age was most influenced by the vegetation type (Figure 7b,e; values of green boxplots) rather than soil type, with the soil type influencing the layer 1 water age most significantly during the recovery period (Figure 7c,f). The higher change in layer 1 water age due to vegetation was not consistent with the change in soil moisture in layer 1 during the drought (more significant change due to soil type, Appendix C). During the recovery period, water ages in layer 2 were most affected by the soil type (Figure 7c,f). However, during the drought, water age in layer 2 was influenced most by soil type in the grassland site (e.g., changing sandy loam to loamy sand under a grassland), while at the forest site the water age in layer 2 was most significantly influenced by vegetation (e.g., changing forest to grassland over a sandy soil). In all periods, the soil layer 3 water age was most affected by the soil type (Figure 7).

4 | DISCUSSION

4.1 | Partitioning of ecohydrologic fluxes in drought and subsequent recovery

The increased likelihood of more frequent and increased severity of extreme drought events in the Northern European Plain intensifies the significance of evaluating water availability in both storage and fluxes under contrasting land-use types (Blenkinsop & Fowler, 2007;

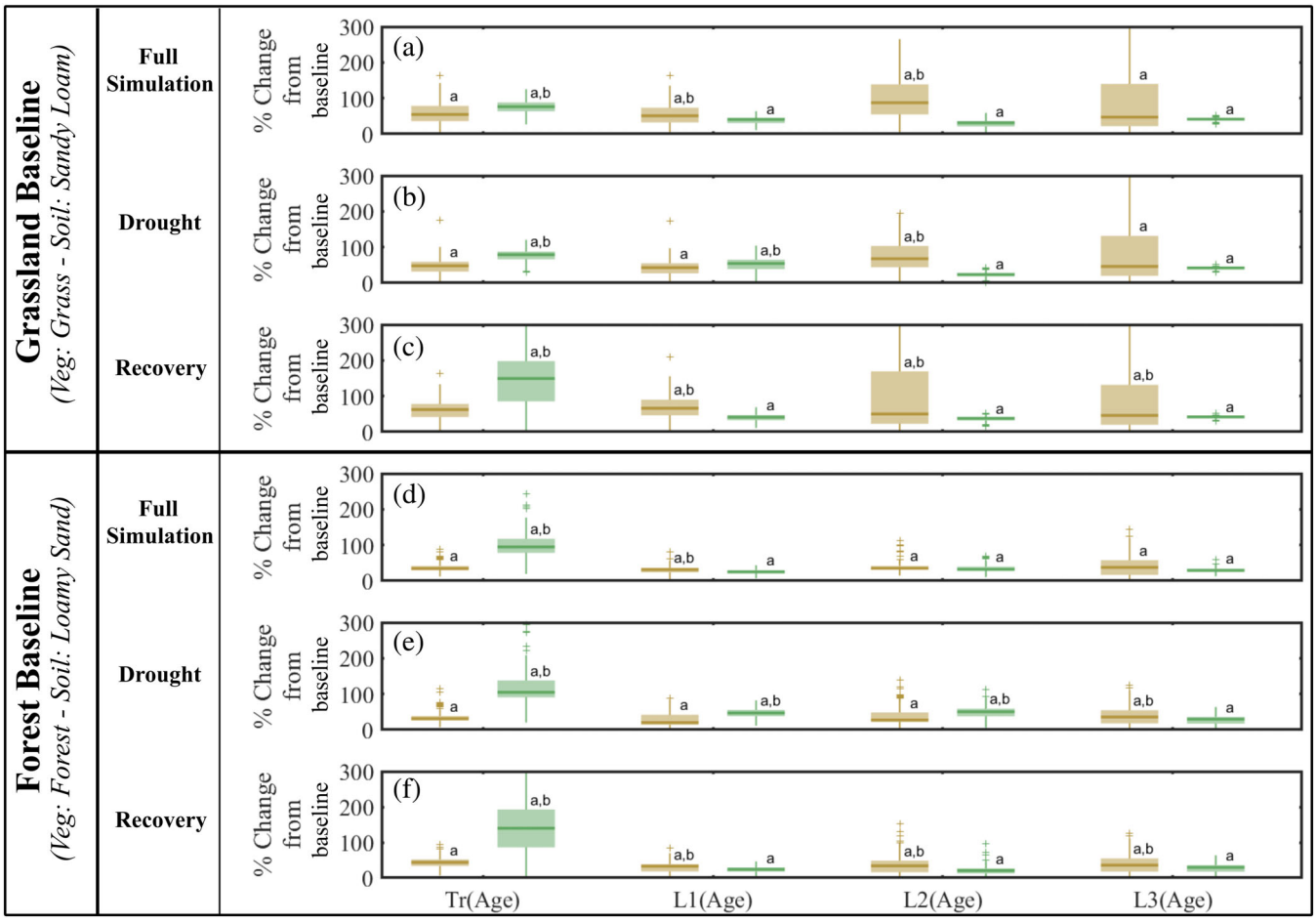

FIGURE 7 Sensitivity of the fluxes and water ages to changes in the soil (brown) and vegetation (green) types relative to the baseline conditions at the forest and grassland sites. Sensitivity is shown as the percent change from the baseline conditions during the (a and d) full simulation, (b and e) drought, and (c and f) recovery periods. The symbol a indicates a significant ($p < .01$) percent change from the baseline and symbol b indicates a significantly ($p < .01$) higher percent change for the flux (comparison of soil and vegetation percent change from baseline)

Hwang et al., 2008). The continued advancements within ecohydrologic modelling, including coupling tracers and water ages with storage and flux interactions (Kuppel et al., 2018a) facilitates a mechanism to evaluate current extreme events and provide a foundation for projecting and mitigating the effects of future extremes.

Climatological conditions in 2018 were extreme relative to long-term measurements with a combination of high temperatures, low relative humidity and precipitation (Figure 2). Low relative humidity and high temperatures maximized the effect of the drought due to increased atmospheric demand for green water losses (higher potential ET, Eslamian, Khordadi, & Abedi-Koupai, 2011) with the only the significant rainfall event in July 2018 (Figure 2a) alleviating the severity. Despite the extreme conditions, the consistency of simulations of soil moisture (Figure 3), energy balance (Figure 4), soil isotopes (Figure 5) and vegetation (Appendix B) to measured dynamics during the drought provide confidence in the skill of the model to capture the main features of ecohydrological functioning under water stress. The flashy and more modulated soil moisture and isotopic response in the forest and grassland site, respectively, are driven more by the soil characteristics than vegetation at each site (Appendix C). The high hydraulic conductivity and lower soil tension in the loamy sand (Dingman, 2002) aids rapid and free-drainage in the forest, compounding with a slower mean increase in near-surface soils wetness (layer 1) relative to the grassland after the drought, but a more rapid response of soil moisture in deeper layers (Figure 2e). There are limitations of EcH_2O-iso that fail to capture all of the moisture dynamics and deficits of deeper soil layers, which is most likely due to the less-robust, but computationally-efficient Green-Ampt soil moisture routing (Rao, Raghuwanshi, & Singh, 2006), with gravitational drainage to lower soil layers (Kuppel et al., 2018b), which may under-estimate water movement through more sandy soils (Ogden & Saghafian, 1997). However, the relatively small estimated error in simulations of uncalibrated soil isotopes provides credible evidence that differences between modelled and measured soil responses at depth are not seriously in error. Furthermore, the crucial differences in the variability of soil moisture between the two sites with depth were captured.

The evaluation of the "blue" and "green" fluxes during the drought suggests further implications of the drought that are not observed solely with the soil moisture dynamics. Both simulations and measurements of transpiration in the forest suggest higher water use for the forest following rainfall events (transpiration simulation, Appendix B), with highly variable (moisture-dependent) transpiration, and low soil evaporation (Barbeta & Peñuelas, 2016; Limousin et al., 2009). The high simulated lc-excess in the forest (Figure 5b) suggests some under-estimation of soil evaporation during the summer, likely following rainfall events when soils were wetter. Some of the under-estimation in soil evaporation may be due to the simulated rapid response in transpiration to precipitation during the drought, which was higher than the sap flow variability. The potential over-estimation of transpiration response following the summer rainfall may be due to a "stress imprint" on vegetation impacting the response of vegetation to water availability (Walter, Jentsch, Beierkuhnlein, & Kreyling, 2013). Under a more extreme event, such as a hypothetical situation where the July 2018 precipitation event had not occurred, more severe water stress conditions for vegetation may result in vegetation mortality (e.g., Allen et al., 2010). While there was some under-estimation of total ET in the forest compared to the MODIS ET data, the MODIS ET data may have bias during dry periods due to the estimation method using vapour pressure deficit as a proxy for water availability for transpiration. The partitioning of the "green" fluxes into transpiration and soil evaporation was more complicated in the grassland due to limitations in measurements of grass transpiration and the use of large-scale MODIS data for calibration. However, the similarities between simulated and observed lc-excess in soil water suggest the model accurately simulated the high estimated soil evaporation fraction of ET. In addition, the high fraction of soil evaporation in ET in the sheltered moderated soil moisture grassland, is similar to the proportions observed in lower energy usage vegetation in a forest canopy understory (e.g., Gobin, Korboulewsky, Dumas, & Balandier, 2015), and sites with (infrequent) vegetation trimming (e.g., Fatichi, Zeeman, Fuhrer, & Burlando, 2014).

Despite the dependence of soil moisture conditions both during the drought and recovery on the soil types, the "blue" fluxes have a strong dependence on both soil and vegetation. The combination of vegetation water usage and sandy soils in the forest limited groundwater recharge to the winter period, consistent with other studies in the region (Douinot et al., 2019). In the grassland, the lower evapotranspiration relative to the forest, along with the slower soil drainage probably explains the more consistent annual groundwater recharge. Disentangling the effect of soil and vegetation on recharge is complex, with vegetation type primarily impacting recharge ("blue" water) during dry conditions (Appendix C). However, vegetation impact on "blue" water fluxes may be lessened where soils are more retentive (higher silt and clay content).

4.2 | Resilience and recovery of soil water ages and ecohydrologic fluxes

The water age dynamics of the forest and grassland sites were comparable to previous studies with younger water in more freely draining soil and older water in more retentive soils (e.g., Tetzlaff, Birkel, Dick, Geris, and Soulsby [2014] and Stumpp, Maloszewski, Stichler, and Fank [2009]); while simultaneously revealing the influence of the drought and recovery on the vulnerability of the vegetation and soils to water limiting conditions. Surprisingly, the shallow soil water age (layer 1, 0–15 cm) did not greatly change progressing through pre-drought, drought, and recovery at either site (Figure 5), which highlights the differences in the reaction of water age and soil moisture to drought. The fractional water ages suggest that the lack of change in mean water age in shallow soils is complex. The mean age estimation is driven by a low soil moisture content which causes a bimodal distribution of young precipitation (increasing the 30-day water fraction, Table 5) and older (with a decreasing volume) stored soil water. With very young water ages in layer 1, it is clear that replenishment by precipitation is a dominant driver in setting water ages. While the moisture content in the shallow soils during the drought is likely driven by

the soil properties at each site (Appendix C), the water age is controlled more by the vegetation than the soil type (Figure 7). This suggests that the type of vegetation has implications for the ability of each site to recover to initial conditions, as older water ages imply longer retention times and slower replenishment of the deeper storages sustaining "blue" water fluxes. Layer 2 at both sites experienced limited percolation and increasing water ages during the drought, with relatively limited change in soil moisture, thus highlighting the vulnerability of sub-soil storage in droughts. In the sandier forest soils, the root-uptake during the drought significantly affected the water ages in layer 2 (Figure 7), and similar to layer 1, has implications for the recovery time of storages sustaining "blue" water fluxes. Similarly, the marked change in root-uptake water ages during the drought suggests that the drought resilience of the plot was approaching a limit. In the loamier grassland site, the much older water present (Table 5) despite the relatively limited change in the mean water age (Table 4) exemplifies the limited percolation of younger water during the drought. Both sites showed a notable lag of 365-day water in layer 2, with higher old water proportions during the recovery period compared to the drought. This lag implies that while the water content appears to have recovered, the system is still under stress from the drought. While the complete mixing assumption used in EcH_2O-iso (Kuppel et al., 2018a) may influence the water ages estimated, the inclusion of incomplete mixing would likely result in greater young water fractions in deeper soils during the wetter recovery period (Kim et al., 2016) and would length the whole system recovery.

Since soil evaporation is sustained by the moisture in the upper soil layer, the effect of evaporation on water ages during the drought is relatively minor. Transpired water ages reveal more distinct differences between the sites. With a notable decrease in transpiration, the water ages of transpiration in the forest during the drought revealed changes in primary water sources from layer 1 to layers 2 and 3 due to physiological changes in the vegetation resulting from extreme water stress in layer 1. With negligible transpiration during the recovery period, the start of the 2019 growing season showed transpiration in the forest rebounding to show a dominance of near-surface (layer 1) water. Despite the relatively consistent transpiration rate in the grassland site, the water ages did not deviate greatly from the water ages in layer 1 suggesting the grass did not experience water stress as severe as the forest. Only a small proportion of transpired water in the grassland originated from layer 2, as evident from the older (>365-day) water (Figure 6h). While the effect of rooting depths on different species transpiration ages has been observed in other regions (Douinot et al., 2019; Kuppel et al., 2018a; Sprenger et al., 2018) the water ages uniquely reveal the vulnerability of the forest vegetation to temporal variation in available waters during drought conditions. These estimates of transpiration age are likely to be conservative as recent work has shown that internal storage and cycling of water by trees may involve additional residence times of several months (Knighton et al., 2020; Köcher, Horna, Beckmeyer, & Leuschner, 2012; Urban, Čermák, & Ceulemans, 2014).

Seeking to provide land and water managers with a quantitative evidence base for building resilience in the face of increased probability of more frequent and intense droughts is the fundamental motivation for integrating empirical measurements and ecohydrologic modelling techniques. A different combination of vegetation and soil could likely reveal wider ranges of resilience in this region, and there is an urgent need for monitoring in contrasting soil-vegetation units and over longer periods (Kundzewicz et al., 2009). Further exploration of either modelling or data-driven analysis could also be used to aid upscaling and developing such understanding to larger management areas (Vereecken, Pachepsky, Bogena, & Montzka, 2019).

5 | CONCLUSION

With the projected increases in the frequency of extreme climate conditions, it is crucial to discern the long-term sustainability of land and water management in drought-sensitive landscapes. This is highly dependent on the partitioning of precipitation into plant available water and water recharging aquifers and sustaining river flows (Orth & Destouni, 2018). Quantifying this partitioning of water, and projecting how it is likely to change, and assessing the resilience of different vegetation and soil systems are during extreme events are all urgent scientific needs. At the grassland and forest plot sites in northeast Germany examined in this study, green water fluxes of evaporation and transpiration were dominant in the summer drought of 2018, with only limited blue water fluxes to groundwater recharge following rainfall events. The loamier soils in the grassland aided in maintaining higher soil moisture and slower response to drought than the sandier soils in the forest. Despite the recovery of soil moisture in the grassland following the drought, fractional water ages in the deeper soil layers suggest that the grassland had not fully recovered from the drought more than half a year after the end of the drought. The sandier forested site had more variable soil moisture, high plant water usage, and stronger young water influence. In the sandier soils, vegetation had a much larger influence on the water age in storage during the drought. Similar to the grassland, fractional water ages indicate a longer recovery period than the soil moisture, though recovery of water ages is less than the grassland (less than half a year). Recharge to the groundwater system under the forest only occurred during the wetter winter period when soil moisture was replenished which coincided with the period of smallest young water fractions and highlights the potential vulnerability of long-term recharge in the forest under future climate scenarios. Utilizing sophisticated tracer-aided ecohydrological models and consideration of water ages can contribute to the evidence base on the hydrologic recovery of "blue" and "green" water fluxes and storage which can inform sustainable land and water management strategies in the future. In this regard, quantifying water use and age dynamics under drought conditions is particularly insightful. Moreover, the research approach adopted in this study provides the potential for further exploration and upscaling of ecohydrological partitioning and resilience to larger catchment scales.

ACKNOWLEDGMENTS

The authors would like to acknowledge the European Research Council for funding the research (project GA 335910 VeWa). The authors

would also like to acknowledge David Dubbert for the isotope analysis. Lastly, the authors thank the University of Aberdeen for the use of the High-Performance Cluster (HPC), which was used for all model runs. The authors thank the issue editor (Paulo Benettin), Stefanie Lutz and two anonymous reviewers for their constructive comments through the review process which has aided in improving the manuscript.

DATA AVAILABILITY STATEMENT

The data that support the findings of this study are available from the corresponding author upon reasonable request.

ORCID

Aaron Smith https://orcid.org/0000-0002-2763-1182
Doerthe Tetzlaff https://orcid.org/0000-0002-7183-8674
Chris Soulsby https://orcid.org/0000-0001-6910-2118

REFERENCES

Allen, C. D., Macalady, A. K., Chenchouni, H., Bachelet, D., McDowell, N., Vennetier, M., … Cobb, N. (2010). A global overview of drought and heat-induced tree mortality reveals emerging climate change risks for forests. *Forest Ecology and Management*, *259*(4), 660–684. https://doi.org/10.1016/j.foreco.2009.09.001

Barbeta, A., & Peñuelas, J. (2016). Sequence of plant responses to droughts of different timescales: Lessons from holm oak (*Quercus ilex*) forests. *Plant Ecology and Diversity*, *9*(4), 321–338. https://doi.org/10.1080/17550874.2016.1212288

Berbel, J., Borrego-Marin, M. M., Exposito, A., Giannoccaro, G., Montilla-Lopez, N. M., & Roseta-Palma, C. (2019). Analysis of irrigation water tariffs and taxes in Europe. *Water Policy*, *21*(4), 806–825. https://doi.org/10.2166/wp.2019.197

Blenkinsop, S., & Fowler, H. J. (2007). Changes in European drought characteristics projected by the PRUDENCE regional climate models. *International Journal of Climatology*, *27*(12), 1595–1610. https://doi.org/10.1002/joc.1538

Christidis, N., Jones, G. S., & Stott, P. A. (2014). Dramatically increasing chance of extremely hot summers since the 2003 European heatwave. *Nature Climate Change*, *5*(1), 46–50. https://doi.org/10.1038/nclimate2468

Dingman, S. L. (2002). Water in soils: Infiltration and redistribution. In *Physical hydrology* (2nd Edition ed., pp. 220–271). Upper Saddle River: Waveland Press.

Douinot, A., Tetzlaff, D., Maneta, M., Kuppel, S., Schulte-Bisping, H., & Soulsby, C. (2019). Ecohydrological modelling with EcH2O-iso to quantify forest and grassland effects on water partitioning and flux ages. *Hydrological Processes*, *33*, 2174–2191. https://doi.org/10.1002/hyp.13480

DWD (2019). CDC (Climate Data Center). Retrieved from https://www.dwd.de/EN/climate_environment/cdc/cdc_node.html

ERA (2019). ERA-Interim. Retrieved from https://www.ecmwf.int/en/forecasts/datasets/reanalysis-datasets/era-interim

Eslamian, S., Khordadi, M. J., & Abedi-Koupai, J. (2011). Effects of variations in climatic parameters on evapotranspiration in the arid and semi-arid regions. *Global and Planetary Change*, *78*(3–4), 188–194. https://doi.org/10.1016/j.gloplacha.2011.07.001

Evaristo, J., Kim, M., Haren, J., Pangle, L. A., Harman, C. J., Troch, P. A., & McDonnell, J. J. (2019). Characterizing the fluxes and age distribution of soil water, plant water, and deep percolation in a model tropical ecosystem. *Water Resources Research*, *55*(4), 3307–3327. https://doi.org/10.1029/2018wr023265

Fatichi, S., Zeeman, M. J., Fuhrer, J., & Burlando, P. (2014). Ecohydrological effects of management on subalpine grasslands: From local to catchment scale. *Water Resources Research*, *50*(1), 148–164. https://doi.org/10.1002/2013wr014535

Fensholt, R., Sandholt, I., & Rasmussen, M. S. (2004). Evaluation of MODIS LAI, fAPAR and the relation between fAPAR and NDVI in a semi-arid environment using in situ measurements. *Remote Sensing of Environment*, *91*(3–4), 490–507. https://doi.org/10.1016/j.rse.2004.04.009

Fritsch, F. N., & Carlson, R. E. (1980). Monotone piecewise cubic interpolation. *SIAM Journal on Numerical Analysis*, *17*, 238–246.

Gobin, R., Korboulewsky, N., Dumas, Y., & Balandier, P. (2015). Transpiration of four common understorey plant species according to drought intensity in temperate forests. *Annals of Forest Science*, *72*(8), 1053–1064. https://doi.org/10.1007/s13595-015-0510-9

Gralher, B., Herbstritt, B., Weiler, M., Wassenaar, L. I., & Stumpp, C. (2018). Correcting for biogenic gas matrix effects on laser-based pore water-vapor stable isotope measurements. *Vadose Zone Journal*, *17*(1), 170157. https://doi.org/10.2136/vzj2017.08.0157

Hanel, M., Rakovec, O., Markonis, Y., Maca, P., Samaniego, L., Kysely, J., & Kumar, R. (2018). Revisiting the recent European droughts from a long-term perspective. *Scientific Reports*, *8*(1), 9499. https://doi.org/10.1038/s41598-018-27464-4

Hrachowitz, M., Savenije, H., Bogaard, T. A., Tetzlaff, D., & Soulsby, C. (2013). What can flux tracking teach us about water age distribution patterns and their temporal dynamics? *Hydrology and Earth System Sciences*, *17*(2), 533–564. https://doi.org/10.5194/hess-17-533-2013

Hwang, T., Kang, S., Kim, J., Kim, Y., Lee, D., & Band, L. (2008). Evaluating drought effect on MODIS gross primary production (GPP) with an eco-hydrological model in the mountainous forest, East Asia. *Global Change Biology*, *14*(5), 1037–1056. https://doi.org/10.1111/j.1365-2486.2008.01556.x

Iglesias, A., & Garrote, L. (2015). Adaptation strategies for agricultural water management under climate change in Europe. *Agricultural Water Management*, *155*, 113–124. https://doi.org/10.1016/j.agwat.2015.03.014

Ivits, E., Horion, S., Fensholt, R., & Cherlet, M. (2014). Drought footprint on European ecosystems between 1999 and 2010 assessed by remotely sensed vegetation phenology and productivity. *Global Change Biology*, *20*(2), 581–593. https://doi.org/10.1111/gcb.12393

Kim, M., Pangle, L. A., Cardoso, C., Lora, M., Volkmann, T. H. M., Wang, Y., … Troch, P. A. (2016). Transit time distributions and StorAge selection functions in a sloping soil lysimeter with time-varying flow paths: Direct observation of internal and external transport variability. *Water Resources Research*, *52*(9), 7105–7129. https://doi.org/10.1002/2016wr018620

King, A. D., & Karoly, D. J. (2017). Climate extremes in Europe at 1.5 and 2 degrees of global warming. *Environmental Research Letters*, *12*(11), 114031. https://doi.org/10.1088/1748-9326/aa8e2c

Kleine, L., Tetzlaff, D., Smith, A., Wang, H., & Soulsby, C. (2020). Using isotopes to understand evaporation, moisture stress and re-wetting in catchment forest and grassland soils of the summer drought of 2018. *Hydrology and Earth System Sciences Discussions*, *2020*, 1–29. https://doi.org/10.5194/hess-2020-81

Kling, H., Fuchs, M., & Paulin, M. (2012). Runoff conditions in the upper Danube basin under an ensemble of climate change scenarios. *Journal of Hydrology*, *424-425*, 264–277. https://doi.org/10.1016/j.jhydrol.2012.01.011

Knighton, J., Kuppel, S., Smith, A., Soulsby, C., Sprenger, M., & Tetzlaff, D. (2020). Using isotopes to incorporate tree water storage and mixing dynamics into a distributed ecohydrologic modelling framework. *Ecohydrology*, *13*, e2201. https://doi.org/10.1002/eco.2201

Köcher, P., Horna, V., Beckmeyer, I., & Leuschner, C. (2012). Hydraulic properties and embolism in small-diameter roots of five temperate broad-leaved tree species with contrasting drought tolerance. *Annals of Forest Science*, *69*(6), 693–703. https://doi.org/10.1007/s13595-012-0189-0

Komatsu, H., Onozawa, Y., Kume, T., Tsuruta, K., Shinohara, Y., & Otsuki, K. (2012). Canopy conductance for a Moso bamboo

(*Phyllostachys pubescens*) forest in western Japan. *Agricultural and Forest Meteorology*, *156*, 111–120. https://doi.org/10.1016/j.agrformet.2012.01.004

Kundzewicz, Z. W., Mata, L. J., Arnell, N. W., DÖLl, P., Jimenez, B., Miller, K., … Shiklomanov, I. (2009). The implications of projected climate change for freshwater resources and their management. *Hydrological Sciences Journal*, *53*(1), 3–10. https://doi.org/10.1623/hysj.53.1.3

Kuppel, S., Tetzlaff, D., Maneta, M. P., & Soulsby, C. (2018a). EcH2O-iso 1.0: Water isotopes and age tracking in a process-based, distributed ecohydrological model. *Geoscientific Model Development*, *11*(7), 3045–3069. https://doi.org/10.5194/gmd-11-3045-2018

Kuppel, S., Tetzlaff, D., Maneta, M. P., & Soulsby, C. (2018b). What can we learn from multi-data calibration of a process-based ecohydrological model? *Environmental Modelling & Software*, *101*, 301–316. https://doi.org/10.1016/j.envsoft.2018.01.001

Landwehr, J. M., & Coplen, T. B. (2006). Line-conditioned excess: A new method for characterizing stable hydrogen and oxygen isotope ratios in hydrologic systems. Paper presented at the international conference on isotopes in environmental studies, International Atomic Energy Agency, Vienna.

Lee, T. J., & Pielke, R. A. (1992). Estimating the soil surface specific humidity. *Journal of Applied Meteorology*, *31*, 480–484.

Limousin, J. M., Rambal, S., Ourcival, J. M., Rocheteau, A., Joffre, R., & Rodriguez-Cortina, R. (2009). Long-term transpiration change with rainfall decline in a Mediterranean*quercus ilex*forest. *Global Change Biology*, *15*(9), 2163–2175. https://doi.org/10.1111/j.1365-2486.2009.01852.x

Maneta, M. P., & Silverman, N. L. (2013). A spatially distributed model to simulate water, energy, and vegetation dynamics using information from regional climate models. *Earth Interactions*, *17*(11), 1–44. https://doi.org/10.1175/2012ei000472.1

Mann, H. B., & Whitney, D. R. (1947). On a test of whether one of two random variables is stochastically larger than the other. *The Annals of Mathematical Statistics*, *18*(1), 50–60.

Mathieu, R., & Bariac, T. (1996). An isotopic study (2H and18O) of water movements in clayey soils under a semiarid climate. *Water Resources Research*, *32*(4), 779–789. https://doi.org/10.1029/96wr00074

McGuire, K. J., DeWalle, D. R., & Gburek, W. J. (2002). Evaluation of mean residence time in subsurface waters using oxygen-18 fluctuations during drought conditions in the mid-Appalachians. *Journal of Hydrology*, *261*, 132–149.

McKee, T., Doesken, N. J., & Kleist, J. (1993). The relationship of drought frequency and duration to time scales. Paper presented at the Eight Conference on Applied Climatology, Anaheim California.

Mein, R. G., & Larson, C. L. (1973). Modeling infiltration during a steady rain. *Water Resources Research*, *9*(2), 384–394.

NASA. (2019a). MODIS leaf area index/FPAR. Retrieved from https://modis.gsfc.nasa.gov/data/dataprod/mod15.php

NASA. (2019b). MODIS/Terra net evapotranspiration 8-day L4 global 500m SIN grid. Retrieved from https://lpdaac.usgs.gov/products/mod16a2v006/

Nash, J. E., & Sutcliffe, J. V. (1970). River flow forecasting through conceptual models part I—A discussion of principles. *Journal of Hydrology*, *10*(3), 282–290. https://doi.org/10.1016/0022-1694(70)90255-6

Newman, B. D., Wilcox, B. P., Archer, S. R., Breshears, D. D., Dahm, C. N., Duffy, C. J., … Vivoni, E. R. (2006). Ecohydrology of water-limited environments: A scientific vision. *Water Resources Research*, *42*(6), W06302. https://doi.org/10.1029/2005wr004141

Ogden, F. L., & Saghafian, B. (1997). Green and Ampt infiltration with redistribution. *Journal of Irrigation and Drainage Engineering*, *123*(5), 386–393. https://doi.org/10.1061/(asce)0733-9437(1997)123:5(386)

Orth, R., & Destouni, G. (2018). Drought reduces blue-water fluxes more strongly than green-water fluxes in Europe. *Nature Communications*, *9*(1), 3602. https://doi.org/10.1038/s41467-018-06013-7

Porporato, A., Laio, F., Ridolif, L., & Rodriguez-Iturbe, I. (2001). Plants in water-controlled ecosystems: Active role in hydrological processes and response to water stress III. Vegetation water stress. *Advances in Water Resources*, *24*, 725–744. https://doi.org/10.1016/S0309-1708(01)00006-9

Quesada, B., Vautard, R., Yiou, P., Hirschi, M., & Seneviratne, S. I. (2012). Asymmetric European summer heat predictability from wet and dry southern winters and springs. *Nature Climate Change*, *2*(10), 736–741. https://doi.org/10.1038/nclimate1536

Rao, M. D., Raghuwanshi, N. S., & Singh, R. (2006). Development of a physically based 1D-infiltration model for irrigated soils. *Agricultural Water Management*, *85*(1–2), 165–174. https://doi.org/10.1016/j.agwat.2006.04.009

Rinaldo, A., Beven, K. J., Bertuzzo, E., Nicotina, L., Davies, J., Fiori, A., … Botter, G. (2011). Catchment travel time distributions and water flow in soils. *Water Resources Research*, *47*(7), W07537. https://doi.org/10.1029/2011wr010478

Rothfuss, Y., Biron, P., Braud, I., Canale, L., Durand, J.-L., Gaudet, J.-P., … Bariac, T. (2010). Partitioning evapotranspiration fluxes into soil evaporation and plant transpiration using water stable isotopes under controlled conditions. *Hydrological Processes*, *24*(22), 3177–3194. https://doi.org/10.1002/hyp.7743

Royer, P. D., Breshears, D. D., Zou, C. B., Cobb, N. S., & Kurc, S. A. (2010). Ecohydrological energy inputs in semiarid coniferous gradients: Responses to management- and drought-induced tree reductions. *Forest Ecology and Management*, *260*(10), 1646–1655. https://doi.org/10.1016/j.foreco.2010.07.036

Schoetter, R., Cattiaux, J., & Douville, H. (2014). Changes of western European heat wave characteristics projected by the CMIP5 ensemble. *Climate Dynamics*, *45*(5–6), 1601–1616. https://doi.org/10.1007/s00382-014-2434-8

Schwalm, C. R., Anderegg, W. R. L., Michalak, A. M., Fisher, J. B., Biondi, F., Koch, G., … Tian, H. (2017). Global patterns of drought recovery. *Nature*, *548*(7666), 202–205. https://doi.org/10.1038/nature23021

Smith, A., Tetzlaff, D., Gelbrecht, J., Kleine, L., & Soulsby, C. (2020). Riparian wetland rehabilitation and beaver re-colonization impacts on hydrological processes and water quality in a lowland agricultural catchment. *Science of the Total Environment*, *699*, 134302. https://doi.org/10.1016/j.scitotenv.2019.134302

Smith, A., Tetzlaff, D., Laudon, H., Maneta, M., & Soulsby, C. (2019). Assessing the influence of soil freeze–thaw cycles on catchment water storage–flux–age interactions using a tracer-aided ecohydrological model. *Hydrology and Earth System Sciences*, *23*(8), 3319–3334. https://doi.org/10.5194/hess-23-3319-2019

Sprenger, M., Stumpp, C., Weiler, M., Aeschbach, W., Allen, S. T., Benettin, P., … Werner, C. (2019). The demographics of water: A review of water ages in the critical zone. *Reviews of Geophysics*, *57*(3), 800–834. https://doi.org/10.1029/2018rg000633

Sprenger, M., Tetzlaff, D., Buttle, J., Carey, S. K., McNamara, J. P., Laudon, H., … Soulsby, C. (2018). Storage, mixing, and fluxes of water in the critical zone across northern environments inferred by stable isotopes of soil water. *Hydrological Processes*, *32*(12), 1720–1737. https://doi.org/10.1002/hyp.13135

Sprenger, M., Tetzlaff, D., & Soulsby, C. (2017). Soil water stable isotopes reveal evaporation dynamics at the soil–plant–atmosphere interface of the critical zone. *Hydrology and Earth System Sciences*, *21*(7), 3839–3858. https://doi.org/10.5194/hess-21-3839-2017

Stoelzle, M., Stahl, K., Morhard, A., & Weiler, M. (2014). Streamflow sensitivity to drought scenarios in catchments with different geology. *Geophysical Research Letters*, *41*(17), 6174–6183. https://doi.org/10.1002/2014gl061344

Stoica, P., & Moses, R. (2005). *Spectral analysis of signals*. Upper Saddle River, NJ: Prentice Hall.

Stumpp, C., Maloszewski, P., Stichler, W., & Fank, J. (2009). Environmental isotope (δ18O) and hydrological data to assess water flow in

unsaturated soils planted with different crops: Case study lysimeter station "Wagna" (Austria). *Journal of Hydrology*, *369*(1–2), 198–208. https://doi.org/10.1016/j.jhydrol.2009.02.047

Sutanto, S. J., Wenninger, J., Coenders-Gerrits, A. M. J., & Uhlenbrook, S. (2012). Partitioning of evaporation into transpiration, soil evaporation and interception: A comparison between isotope measurements and a HYDRUS-1D model. *Hydrology and Earth System Sciences*, *16*(8), 2605–2616. https://doi.org/10.5194/hess-16-2605-2012

Tetzlaff, D., Birkel, C., Dick, J., Geris, J., & Soulsby, C. (2014). Storage dynamics in hydropedological units control hillslope connectivity, runoff generation, and the evolution of catchment transit time distributions. *Water Resources Research*, *50*(2), 969–985. https://doi.org/10.1002/2013WR014147

Tetzlaff, D., Buttle, J., Carey, S. K., van Huijgevoort, M. H., Laudon, H., McNamara, J. P., … Soulsby, C. (2015). A preliminary assessment of water partitioning and ecohydrological coupling in northern headwaters using stable isotopes and conceptual runoff models. *Hydrological Processes*, *29*(25), 5153–5173. https://doi.org/10.1002/hyp.10515

Teuling, A. J., Seneviratne, S. I., Stöckli, R., Reichstein, M., Moors, E., Ciais, P., … Wohlfahrt, G. (2010). Contrasting response of European forest and grassland energy exchange to heatwaves. *Nature Geoscience*, *3*(10), 722–727. https://doi.org/10.1038/ngeo950

Thomas, B., Lischeid, G., Steidl, J., & Dietrich, O. (2015). Long term shift of low flows predictors in small lowland catchments of Northeast Germany. *Journal of Hydrology*, *521*, 508–519. https://doi.org/10.1016/j.jhydrol.2014.12.022

Toreti, A., Belward, A., Perez-Dominguez, I., Naumann, G., Luterbacher, J., Cronie, O., … Zampieri, M. (2019). The exceptional 2018 European water seesaw calls for action on adaptation. *Earth's Future*, *7*(6), 652–663. https://doi.org/10.1029/2019ef001170

Trombetta, A., Iacobellis, V., Tarantino, E., & Gentile, F. (2016). Calibration of the AquaCrop model for winter wheat using MODIS LAI images. *Agricultural Water Management*, *164*, 304–316. https://doi.org/10.1016/j.agwat.2015.10.013

UGT (2019). SMT-100. Retrieved from https://www.ugt-online.de/en/products/soil-science/soil-moisture/smt-100/

Urban, J., Čermák, J., & Ceulemans, R. (2014). Above- and below-ground biomass, surface and volume, and stored water in a mature scots pine stand. *European Journal of Forest Research*, *134*(1), 61–74. https://doi.org/10.1007/s10342-014-0833-3

Vereecken, H., Pachepsky, Y., Bogena, H., & Montzka, C. (2019). Upscaling issues in ecohydrological observations. In X. Li & H. Vereecken (Eds.), *Observation and measurement of ecohydrological processes* (pp. 435–454). Berlin, Heidelberg: Springer Berlin Heidelberg.

Vogt, H. J. (1976). Isotopentrennung bei der Verdunstung von Wasser, Staatsexamensarbeit. Heidelberg, Germany.

Walter, J., Jentsch, A., Beierkuhnlein, C., & Kreyling, J. (2013). Ecological stress memory and cross stress tolerance in plants in the face of climate extremes. *Environmental and Experimental Botany*, *94*, 3–8. https://doi.org/10.1016/j.envexpbot.2012.02.009

Walter, J., Nagy, L., Hein, R., Rascher, U., Beierkuhnlein, C., Willner, E., & Jentsch, A. (2011). Do plants remember drought? Hints towards a drought-memory in grasses. *Environmental and Experimental Botany*, *71*(1), 34–40. https://doi.org/10.1016/j.envexpbot.2010.10.020

Wassenaar, L., Hendry, M. J., Chostner, V. L., & Lis, G. P. (2008). High resolution pore water δ2H and δ18O measurements by H2O(liquid)–H2O(vapor) equilibration laser spectroscopy. *Environmental Science & Technology*, *42*(24), 9262–9267. https://doi.org/10.1021/es802065s

SUPPORTING INFORMATION

Additional supporting information may be found online in the Supporting Information section at the end of this article.

How to cite this article: Smith A, Tetzlaff D, Kleine L, Maneta MP, Soulsby C. Isotope-aided modelling of ecohydrologic fluxes and water ages under mixed land use in Central Europe: The 2018 drought and its recovery. *Hydrological Processes*. 2020;34:3406–3425. https://doi.org/10.1002/hyp.13838